Reactor ν[over ¯]_{e} disappearance in the Double Chooz experiment

Y. Abe *et al.* (Double Chooz Collaboration)

Reactor $\bar{\nu}_e$ disappearance in the Double Chooz experiment

Y. Abe,[30] C. Aberle,[21] J.C. dos Anjos,[5] J.C. Barriere,[15] M. Bergevin,[9] A. Bernstein,[16] T.J.C. Bezerra,[28]
L. Bezrukhov,[14] E. Blucher,[6] N.S. Bowden,[16] C. Buck,[21] J. Busenitz,[2] A. Cabrera,[4] E. Caden,[10] L. Camilleri,[8]
R. Carr,[8] M. Cerrada,[7] P.-J. Chang,[17] P. Chimenti,[33] T. Classen,[9, 16] A.P. Collin,[15] E. Conover,[6] J.M. Conrad,[20]
J.I. Crespo-Anadón,[7] K. Crum,[6] A. Cucoanes,[25, 15] M.V. D'Agostino,[3] E. Damon,[10] J.V. Dawson,[4, 36] S. Dazeley,[16]
D. Dietrich,[32] Z. Djurcic,[3] M. Dracos,[24] V. Durand,[15, 4] J. Ebert,[11] Y. Efremenko,[27] M. Elnimr,[25] A. Etenko,[19]
M. Fallot,[25] M. Fechner,[15] F. von Feilitzsch,[26] J. Felde,[9] D. Franco,[4] A.J. Franke,[8] M. Franke,[26] H. Furuta,[28]
R. Gama,[5] I. Gil-Botella,[7] L. Giot,[25] M. Göger-Neff,[26] L.F.G. Gonzalez,[34] M.C. Goodman,[3] J.TM. Goon,[2]
D. Greiner,[32] N. Haag,[26] C. Hagner,[11] T. Hara,[18] F.X. Hartmann,[21] J. Haser,[21] A. Hatzikoutelis,[27] T. Hayakawa,[22]
M. Hofmann,[26] G.A. Horton-Smith,[17] A. Hourlier,[4] M. Ishitsuka,[30] J. Jochum,[32] C. Jollet,[24] C.L. Jones,[20]
F. Kaether,[21] L.N. Kalousis,[24] Y. Kamyshkov,[27] D.M. Kaplan,[13] T. Kawasaki,[22] G. Keefer,[16] E. Kemp,[34] H. de
Kerret,[4, 36] Y. Kibe,[30] T. Konno,[30] D. Kryn,[4] M. Kuze,[30] T. Lachenmaier,[32] C.E. Lane,[10] C. Langbrandtner,[21]
T. Lasserre,[15, 4] A. Letourneau,[15] D. Lhuillier,[15] H.P. Lima Jr,[5] M. Lindner,[21] J.M. López-Castano,[7]
J.M. LoSecco,[23] B.K. Lubsandorzhiev,[14] S. Lucht,[1] D. McKee,[17] J. Maeda,[31] C.N. Maesano,[9] C. Mariani,[8, 35]
J. Maricic,[10] J. Martino,[25] T. Matsubara,[31] G. Mention,[15] A. Meregaglia,[24] T. Miletic,[10] R. Milincic,[10] H. Miyata,[22]
Th.A. Mueller,[28] Y. Nagasaka,[12] K. Nakajima,[22] P. Novella,[7] M. Obolensky,[4] L. Oberauer,[26] A. Onillon,[25]
A. Osborn,[27] I. Ostrovskiy,[2] C. Palomares,[7] I.M. Pepe,[5] S. Perasso,[10] P. Perrin,[15] P. Pfahler,[26] A. Porta,[25]
W. Potzel,[26] J. Reichenbacher,[2] B. Reinhold,[21] A. Remoto,[25, 4] M. Röhling,[32] R. Roncin,[4] S. Roth,[1] Y. Sakamoto,[29]
R. Santorelli,[7] F. Sato,[31] S. Schönert,[26] S. Schoppmann,[1] T. Schwetz,[21] M.H. Shaevitz,[8] S. Shimojima,[31]
D. Shrestha,[17] J-L. Sida,[15] V. Sinev,[14, 15] M. Skorokhvatov,[19] E. Smith,[10] J. Spitz,[20] A. Stahl,[1] I. Stancu,[2]
L.F.F. Stokes,[32] M. Strait,[6] A. Stüken,[1] F. Suekane,[28] S. Sukhotin,[19] T. Sumiyoshi,[31] Y. Sun,[2] R. Svoboda,[9]
K. Terao,[20] A. Tonazzo,[4] M. Toups,[8] H.H. Trinh Thi,[26] G. Valdiviesso,[5] C. Veyssiere,[15] S. Wagner,[21] H. Watanabe,[21]
B. White,[27] C. Wiebusch,[1] L. Winslow,[20] M. Worcester,[6] M. Wurm,[11] F. Yermia,[25] and V. Zimmer[26]

(Double Chooz Collaboration)

[1]*III. Physikalisches Institut, RWTH Aachen University, 52056 Aachen, Germany*
[2]*Department of Physics and Astronomy, University of Alabama, Tuscaloosa, Alabama 35487, USA*
[3]*Argonne National Laboratory, Argonne, Illinois 60439, USA*
[4]*APC, AstroParticule et Cosmologie, Université Paris Diderot, CNRS/IN2P3,
CEA/IRFU, Observatoire de Paris, Sorbonne Paris Cité, 75205 Paris Cedex 13, France*
[5]*Centro Brasileiro de Pesquisas Físicas, Rio de Janeiro, RJ, cep 22290-180, Brazil*
[6]*The Enrico Fermi Institute, The University of Chicago, Chicago, IL 60637, USA*
[7]*Centro de Investigaciones Energéticas, Medioambientales y Tecnológicas, CIEMAT, E-28040, Madrid, Spain*
[8]*Columbia University; New York, NY 10027, USA*
[9]*University of California, Davis, CA-95616-8677, USA*
[10]*Physics Department, Drexel University, Philadelphia, Pennsylvania 19104, USA*
[11]*Institut für Experimentalphysik, Universität Hamburg, 22761 Hamburg, Germany*
[12]*Hiroshima Institute of Technology, Hiroshima, 731-5193, Japan*
[13]*Department of Physics, Illinois Institute of Technology, Chicago, Illinois 60616, USA*
[14]*Institute of Nuclear Research of the Russian Academy of Science, Russia*
[15]*Commissariat à l'Energie Atomique et aux Energies Alternatives, Centre de Saclay, IRFU, 91191 Gif-sur-Yvette, France*
[16]*Lawrence Livermore National Laboratory, Livermore, CA 94550, USA*
[17]*Department of Physics, Kansas State University, Manhattan, Kansas 66506, USA*
[18]*Department of Physics, Kobe University, Kobe, 657-8501, Japan*
[19]*NRC Kurchatov Institute, 123182 Moscow, Russia*
[20]*Massachusetts Institute of Technology; Cambridge, MA 02139, USA*
[21]*Max-Planck-Institut für Kernphysik, 69117 Heidelberg, Germany*
[22]*Department of Physics, Niigata University, Niigata, 950-2181, Japan*
[23]*University of Notre Dame, Notre Dame, IN 46556- 5670, USA*
[24]*IPHC, Université de Strasbourg, CNRS/IN2P3, F- 67037 Strasbourg, France*
[25]*SUBATECH, CNRS/IN2P3, Université de Nantes, Ecole des Mines de Nantes, F-44307 Nantes, France*
[26]*Physik Department, Technische Universität München, 85747 Garching, Germany*
[27]*Department of Physics and Astronomy, University of Tennessee, Knoxville, Tennessee 37996, USA*
[28]*Research Center for Neutrino Science, Tohoku University, Sendai 980-8578, Japan*
[29]*Tohoku Gakuin University, Sendai, 981-3193, Japan*
[30]*Department of Physics, Tokyo Institute of Technology, Tokyo, 152-8551, Japan*
[31]*Department of Physics, Tokyo Metropolitan University, Tokyo, 192-0397, Japan*
[32]*Kepler Center for Astro and Particle Physics, Universität Tübingen, 72076, Tübingen, Germany*
[33]*Universidade Federal do ABC, UFABC, Saõ Paulo, Santo André, SP, Brazil*

[34] *Universidade Estadual de Campinas-UNICAMP, Campinas, SP, Brazil*
[35] *Center for Neutrino Physics, Virginia Tech, Blacksburg, VA*
[36] *Laboratoire Neutrino de Champagne Ardenne, domaine d'Aviette, 08600 Rancennes, France*

The Double Chooz experiment has observed 8,249 candidate electron antineutrino events in 227.93 live days with 33.71 GW-ton-years (reactor power × detector mass × livetime) exposure using a 10.3 m^3 fiducial volume detector located at 1050 m from the reactor cores of the Chooz nuclear power plant in France. The expectation in case of $\theta_{13}= 0$ is 8,937 events. The deficit is interpreted as evidence of electron antineutrino disappearance. From a rate plus spectral shape analysis we find $\sin^2 2\theta_{13} = 0.109 \pm 0.030(\text{stat}) \pm 0.025(\text{syst})$. The data exclude the no-oscillation hypothesis at 99.8% CL (2.9σ).

I. INTRODUCTION

In the three neutrino paradigm, there are three mixing angles that can be measured in neutrino oscillation experiments. For many years, the CHOOZ reactor neutrino experiment [1] had the best limit on the value of θ_{13}. Recently, the value of θ_{13} has been shown to be non-zero by the combination of fits to KamLAND and solar [2–4], MINOS [5], T2K [6] and, more precisely, by the new generation of reactor antineutrino disappearance experiments: Double Chooz [7], Daya Bay [8] and RENO [9].

The Double Chooz analysis is unique among reactor experiments in its fit to the energy spectrum. In the previous reactor measurements of θ_{13}, Double Chooz presented both a rate-only analysis and an analysis using both the rate and the shape of the energy spectrum, while Daya Bay and RENO presented rate-only analyses. The disappearance of reactor electron antineutrinos has a well-defined effect on the shape of that spectrum. The use of the energy distribution to constrain the oscillation parameters requires a good understanding of the energy response of the detector and of the accuracy of the Monte Carlo. That understanding is achieved through multiple calibration techniques, in time, space and energy.

This paper continues the analysis reported in [7] with a larger data set, a new energy scale definition, reduced background rates and improved systematic uncertainties. Additionally, the running period has been subdivided into a two-reactor-on period and a one-reactor-on period in the oscillation fit to help separate signal and background.

Reactor antineutrinos are observed using the inverse beta decay (IBD) reaction $\bar{\nu}_e + p \rightarrow e^+ + n$ in which there is a positron whose signal is promptly seen, and a neutron, whose delayed signal is seen after a mean time of about 30 μs from its capture in the gadolinium-doped target. The prompt energy of the positron allows us to determine the antineutrino energy and observe the antineutrino spectrum. The energy deposited by the positron including annihilation is related to antineutrino energy $E_{\bar{\nu}_e}$ by $E_{\text{prompt}} = E_{\bar{\nu}_e} - T_n - 0.8$ MeV where T_n denotes the average neutron recoil energy and is small compared to $E_{\bar{\nu}_e}$.

The previous analysis represented 15.34 GW-ton-years of exposure, taking into account the reactor livetime and the detector fiducial mass. Here we re-analyze that data set together with an additional 18.37 GW-ton-years giving a total of 33.71 GW-ton-years. In addition the analysis of 22.5 hours of both-reactors-off data allows a cross check of our estimates of the correlated and accidental backgrounds.

The structure of the paper is as follows. In Section II we review the experimental setup and detector. Section III covers the measurements and simulations of the Chooz reactors used to predict the unoscillated neutrino spectrum, as well as the model used to describe the detector. Event reconstruction including the energy determination of candidate events is described in Section IV. The steps that are used to identify reactor neutrino candidates are covered in Section V. Section VI presents the extraction of neutrino mixing parameters from the measured antineutrino rate and energy distribution.

II. DETECTOR AND METHOD DESCRIPTION

A. Overview

The Double Chooz detector system [10] consists of a main detector, an outer veto, and calibration devices (Figure 1). The main detector is made of four concentric cylindrical tanks with a chimney in the center at the top and is filled with liquid scintillators or mineral oil.

The innermost 8 mm thick transparent (UV to visible) acrylic vessel contains 10.3 m^3 gadolinium loaded liquid scintillator called the ν-target (NT). The NT volume is surrounded by the γ-catcher (GC), a 55 cm thick Gd-free liquid scintillator layer in a second 12 mm thick acrylic vessel, used to detect gamma rays escaping from the ν-target. Outside the γ-catcher is the buffer, a 105 cm thick mineral oil layer. It shields from radioactivity of photomultiplier tubes (PMTs) and surrounding rock, and is one of the major improvements over the CHOOZ experiment [1]. The 390 10-inch PMTs [11–13] are installed on the inner wall of the stainless steel buffer tank to collect light from the inner volumes. These three volumes and PMTs constitute central detector system referred to as the inner detector (ID). Outside the ID, and optically separated from it by a stainless steel vessel, is a 50 cm

thick inner veto (IV) liquid scintillator. It is equipped with 78 8-inch PMTs and functions as a cosmic muon veto and as an active shield to spallation neutrons produced outside the detector. The detector is covered and surrounded by 15 cm of demagnetized steel to suppress external gamma rays. The main detector is covered by an outer veto system (OV) described in Section II G.

B. Radiopurity

All parts of the Double Chooz detector have been thoroughly screened for their content of radioactive isotopes prior to their installation. The screening was carried out by direct gamma spectroscopy with a variety of germanium detectors in underground laboratories. Among them were the large HPGe detector for the non-destructive radioassay at Saclay [14] and the GeMPI detector at Gran Sasso [15] with a sensitivity of about $10\,\mu$Bq/kg for U and Th. In addition, neutron activation analyses have been performed for dedicated parts of the inner detector: the acrylics for NT and GC vessels as well as the wavelength shifter PPO [16]. The irradiations were done at the FRM II research reactor in Garching, Germany by a thermal neutron flux of $1.63\cdot10^{13}\,\mathrm{cm}^{-2}\cdot\mathrm{s}^{-1}$, with subsequent gamma spectroscopy in the Garching underground laboratory [17].

The PMT glass and cavern rock are the main sources of the gamma ray background. The PMT glass was made from low activity sands using a platinum coated furnace to reduce contamination. Radioactivity of the glass samples was measured during development of the low activity glass and production of the PMTs [18]. The average measurements were 13 ppb, 61 ppb and 3.3 ppb for ^{238}U,
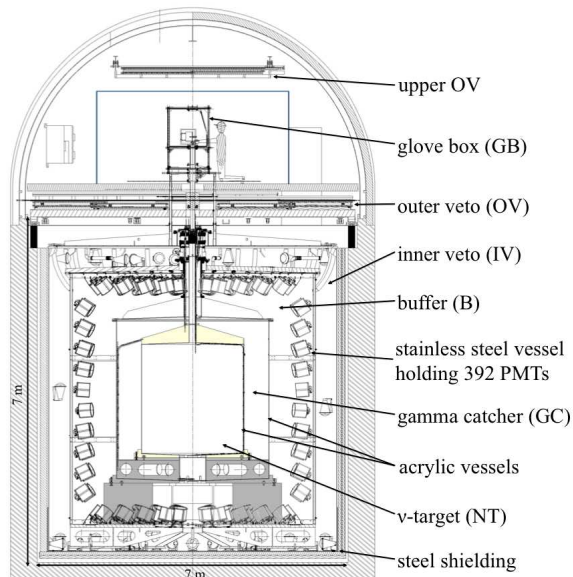

FIG. 1. A cross-sectional view of the Double Chooz detector system.

^{232}Th and ^{40}K, respectively assuming radio-equilibrium, which are much smaller than regular PMT glass.

The design goal of Double Chooz concerning radiopurity is no more than $\sim$0.8 accidental background events per day. Along with the radiopurity screenings, Double Chooz maintained strict clean-room conditions during the setup of the detector with an ISO-level up to 6. The analysis of BiPo coincidences in the detector data yields concentrations of U and Th in NT and GC below the design goal of 10^{-13} g/g. The accidentals rate is measured to be < 0.5 d^{-1}, well below our design goal. The daily rate of correlated background events stemming from (α, n)-reactions of ^{210}Po on ^{13}C is estimated to be smaller than 0.020 d^{-1} (scaled from the result of Kam-LAND [19]), which is negligibly small compared to the neutrino signal.

C. Double Chooz Liquids

The CHOOZ experiment was limited in sensitivity by the optical instability of its gadolinium-loaded (Gd) scintillator [20]. Therefore a new type of metal loaded organic liquid scintillator was developed for Double Chooz [16]. The target scintillator used in the NT must fulfill the basic requirements of Gd solubility in the solvent of choice, optical transparency, radiopurity and chemical stability. In addition, the organic liquid must be compatible with the detector materials in contact with the scintillator, mainly acrylics. Safety considerations influenced the scintillator design as well.

Since the rare earth Gd does not dissolve in the required amount in the organic solvents used for liquid scintillators, a metalorganic complex is formed providing higher solubility. In particular, the complex of choice is a metal-β-diketone, Gd(thd)$_3$, Gd(III)-tris-(2,2,6,6-tetramethyl-heptane-3,5-dionate). Such complexes are known for their stability and high vapor pressure. This allowed us to purify the material by sublimation reducing radioimpurities U, Th and K. The Gd concentration in the NT is 0.123% by weight, which corresponds to about 1 g/liter.

As scintillator solvent for the NT we have chosen an ortho-phenylxylylethane (o-PXE)/n-dodecane mixture at a volume ratio of 20/80. To shift the scintillation light into a more transparent region, wavelength shifters are added. In both scintillators we use PPO (2,5-diphenyloxazole) as primary fluor and bis-MSB (4-bis-(2-methylstyryl)benzene) as secondary wavelength shifter.

The light yield and density of the GC liquid (22.5 m^3) were matched simultaneously to the NT values [21]. To achieve this goal, a medicinal white oil was added as a third solvent to the GC. The light yield of the GC is optimized for homogeneous detector response using Monte Carlo simulations. To avoid mechanical stress on the detector vessels the densities of all four detector liquids were matched at the detector temperature of about 15 °C to $0.804\ \pm\ 0.001$ g/cm^3.
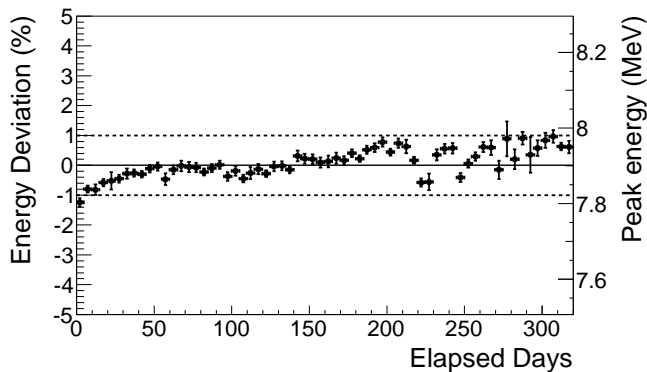
FIG. 2. Average target detector response evolution in time, as measured by the mean energy of the Gd-capture peak arising from interaction of spallation neutrons in the NT.

The attenuation lengths for wavelengths in the region of scintillator emission are well above the dimensions of the corresponding vessels. Optical stability of the scintillators is demonstrated in Figure 2, where the stability of the peak energy of neutron captures on Gd is shown. The energy response of the detector was found to be stable within 1% over the data-taking period of about one year.

The absolute number of H nuclei ("proton number") as well as the precision on its knowledge are crucial parameters. The error on the proton number is minimized by using well defined and pure chemicals in combination with a precise knowledge of the weights of each chemical added in the scintillator production. The amount of NT scintillator was determined after thermalization by a weight measurement with a precision of 0.04%. The hydrogen fraction in the NT is 13.6% by weight, known with 0.3% relative precision. This error includes the uncertainties originating from the weights of the scintillator ingredients. In addition, the error takes into account the knowledge of the hydrogen content of not fully defined impurities in the chemicals which are on the per mil level for the main components [16].

A mixture of solvents was used in all detector volumes to allow for density matching. The 110 m³ of buffer liquid contain a medicinal white oil (53% by volume) and an n-alkane mixture (47% by volume). This liquid was optimized for transparency and low aromaticity to minimize scintillation light production in the buffer. The veto volume is filled with 90 m³ of liquid scintillator, a mixture of linear alkyl benzene (LAB) and n-alkanes, with 2 g/l PPO as fluor and 20 mg/l bis-MSB as secondary wavelength shifter.

D. ID Photomultiplier Tubes

The inner detector uses 390 Hamamatsu R7081 10-inch PMTs [22] to view the target volume. The glass is a low

background type, contributing only a few Hz of singles rate in the detector. The PMTs are operated with a gain of 10^7 at the PMT anode. They are submerged in a paraffin oil buffer liquid. The base circuit is enclosed in a transparent epoxy resin. Some PMTs are observed to generate light flashes from their base circuit through the epoxy resin, causing false triggers. HV for the 14 worst PMTs was turned off. Since the signal pattern is different from that of the neutrino signal, the false events are safely removed from the neutrino sample as described in Section IV D. The 800 PMTs for both this and an eventual near detector were characterized carefully [11, 12, 23]. The following characteristics were measured: for one photoelectron signals, the ratio of the one photoelectron peak to the valley between that peak and the pedestal was 4, with 1/4 photoelectron thresholds; the quantum efficiency × collection efficiency (efficiency that photoelectrons produced in the cathode are collected by the first dynode) was 23%; transit time spread was 3 ns (FWHM); the afterpulse probability was in average 2.7%; the charge output was linear up to 300 photoelectrons per PMT; dark hit rate was approximately 2 kHz measured 20 hours after turning on the HV. Each PMT is shielded by a mu-metal cylinder to suppress effects from the gamma shield and the earth's magnetic field [13] and is equipped with an angle-adjustable mounting jig. The PMTs are angled to collect light more uniformly from the detector.

E. The Inner Veto

The IV is a cylindrical stainless steel vessel (radius 3.3 m and height 6.8 m) surrounding the ID and optically separated by the buffer tank. It shields the ID with a 50 cm thick layer of liquid scintillator against external radioactivity and spallation neutrons created by cosmic muons. At the same time it acts as an active detector identifying cosmic muons crossing it. The design of the IV was optimized by the use of a MC simulation [24], where the emphasis was on a high number of detected photoelectrons (PE) per MeV deposited in the IV volume and on a high efficiency in rejecting muons and correlated background events produced by them. The resulting configuration of the IV consists of 78 PMTs, divided into three parts: the top has 24 PMTs, the side walls have 12 PMTs at the mid way point and the bottom has 42 PMTs. The 78 8-inch PMTs (Hamamatsu R 1408), which were previously used in the IMB and Super-Kamiokande experiments, were tested and modified for use in Double Chooz [25]. Each IV PMT and its base are contained in a stainless steel encapsulation, with a transparent PET window at the front end. The capsules are filled with mineral oil to match the optical properties of the surrounding scintillator. All surfaces of the IV are painted with highly reflective white coating (AR100/CLX coating from MaxPerles [26]), the side walls of the buffer vessel are covered with reflective

VM2000 sheets. Using the OV, the muon rejection efficiency was found to be larger than 99.99 % for muons crossing the IV volume.

F. Electronics and Data Acquisition

The full readout and data acquisition (DAQ) for both the ID and the IV detectors are depicted in Figure 3. The functional principle is that digitization of PMT signals (see Section II D) is done by flash-ADC electronics. As shown in Figure 3, from left to right, the electronics elements are the High Voltage (HV) splitter, the HV supply, the Front-End electronics (FEE), the Trigger system [27] and the flash-ADC digitizing electronics [28, 29] (ν-FADC). Each PMT has a single cable for both PMT signal (5 mV per PE) and HV (~ 1.3 kV). A custom made HV-splitter circuit decouples both components. The HV is provided by CAEN-A1535P [30] supplies. PMT signals are optimized (amplified, clipped, baseline restored and coherent noise filtered) by the FEE for digitization. The FEE also delivers sum signals, whose amplitude is proportional to charge, that are fed into a custom trigger system. The circuit generating the sum signal subtracts the input amplitude after about 100 ns. This capability allows the trigger input signals to suffer from minimal overshoot that can lead to trigger dead-time. This same feature works as a high-pass filter: slow signals (frequency $\lesssim 1$ MHz) cannot cause a trigger. The ID PMTs are separated into two ID super-groups at the trigger level, uniformly distributed across the volume. Either super-group can cause a trigger of the ID based on energy and sub-group multiplicity information. The ID triggers at energies about 350 keV. The trigger efficiency is 100.0% above the analysis threshold 0.7 MeV with negligible uncertainty. Both energy and sub-group multiplicity information are used to cause IV triggers. The IV triggers at ~ 10 MeV which corresponds to 8 cm of a minimum ionizing muon track. The ν-FADC system relies on 64 CAEN-Vx1721(VME64x) [30] waveform digitizers. Each card has 8 channel with 8-bit flash-ADC (FADC) at 500 MS/s. Each channel holds up to 1024 4 μs waveforms without readout. When triggered, the 256 ns waveform is recorded, containing $> 90\%$ of the scintillation light emitted. Up to ~ 3 MeV, a single-PE is deposited per channel, each having ~ 40 mV amplitude corresponding to around 10 samples per PE. FADC amplitude saturation leads to some degree of non-linearity for > 100 MeV energies. Above 500 MeV, up to a 40% non-linearity has been estimated.

The FADC baselines are observed to be stable, showing variations below 1 ADC. After power-cycling, small (sub-mV) DC shifts in the baseline are observed. Due to under-sampling of the baseline, these shifts can cause a bias in the reconstructed charge estimation. This bias manifests itself as an effective non-linearity for signals below 2 PEs and has been thoroughly studied, measured and calibrated out, as described in Section Section IV E.
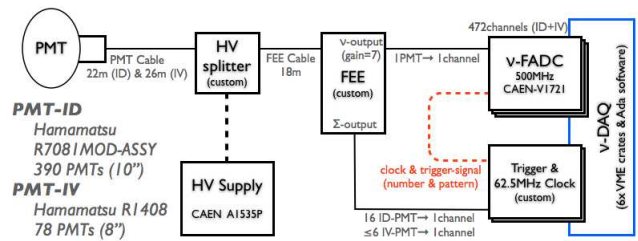

FIG. 3. Block diagram of the Double Chooz readout and DAQ systems.

All systems (trigger, ID and IV) are readout by the same DAQ upon any trigger of either the ID or IV. The system is deadtime free, as demonstrated by two monitor systems running at 2 Hz. The dead time monitor waveforms are, in addition, used to randomly sample the detector providing extra baseline monitoring, background and dark-current information.

G. The Outer Veto

The OV is installed above the ID, IV and 15 cm of shielding steel. A lower outer veto is mounted directly above the shielding and provides (x, y) coordinate for muons passing through a 13 m × 7 m area centered on the chimney; a 110 cm × 30 cm region around the chimney is left open. The lower outer veto has been installed for 68.9% of the data presented here, and is used to help reduce background levels quoted in [7]. An upper outer veto, again measuring (x, y) coordinates, has been mounted above the chimney and glove box used for source insertion, to cover this area. The upper outer veto was not present for this analysis.

The outer veto is assembled from modules containing 64 scintillator strips, each 5 cm × 1 cm × 320 cm or 360 cm. Each strip was extruded with a hole running through its length, through which a 1.5 mm diameter wavelength-shifting fiber was threaded. Modules are built out of two superimposed 32-strip layers with the top layer offset by 2.5 cm from the bottom layer. The 64 fibers are coupled at one end to a Hamamatsu H8804 multi-anode photomultiplier tube (M64); the other fiber ends are mirrored. The OV modules are positioned over the inner detector in two layers, one with strips oriented in the x direction and one in the y direction. Each M64 is connected to a custom front-end board with a MAROC2 ASIC [31] and an FPGA. The MAROC2 allows adjustment of the electronic gain of each of the 64 channels, which is needed to correct for the factor of 2 pixel-to-pixel gain variation in the M64. Signals that exceed a common threshold are sent to a multiplexed 12-bit ADC, providing charge information for hit strips.

H. Calibration Systems

The experiment is calibrated using light sources, radioactive (point-like) sources, and cosmic rays.

A multi-wavelength LED–fiber system (LI) is used to inject light into the inner detector and the inner veto from a set of fixed points. The optical fibers of the LI are routed inside the detector and the fiber ends are attached to the PMT covers. Some of the injection points are equipped with diffuser plates to widely illuminate the detector. The other ends of the fibers are connected to blue and UV LEDs (385, 425 and 470 nm wavelengths for the ID, and 365 and 475 nm for the IV) whose flash rate, light intensity and pulse width are controlled remotely. Data are taken with the LI systems regularly. The LI data are used to measure the PMT and readout electronics gains and the time offsets and to monitor the stability of those gains and offsets.

Radio-isotopes ^{137}Cs, ^{68}Ge, ^{60}Co, and ^{252}Cf, sealed in miniature capsules, have been deployed in the NT and GC. The visible energy response is measured with a 0.662 MeV gamma (Cs–137), 2×0.511 MeV annihilation gammas (Ge–68), which also corresponds to the threshold for inverse beta decay, the combination of 1.173 MeV and 1.333 MeV gammas (Co–60), and the 2.223 MeV gamma from neutron capture on hydrogen (Cf–252). The detector response to neutrons is calibrated using ^{252}Cf. Source rates are at the level of 50 Bq.

Deployments in the NT are realized by lowering the sources from a glove box at the detector top through the detector chimney. A motorized pulley-and-weight system, operated from a glove box, is used to position sources at positions along the target symmetry axis. The range of deployments is from 1 cm above the NT bottom up to the chimney; the positions of the source are known within 1 mm. In the GC, the source is attached to a motor-driven wire and guided through a rigid hermetic looped tube (GT). The sources are inserted in the GT near the chimney top. The loop traverses interior regions of the GC and passes near boundaries with the NT and the buffer. The position of the source along the loop is known to 1 cm, and in the NT boundary region, the perpendicular distance between the source and the target wall is known within 2 mm. The materials of the source capsules and deployment systems in the NT and GC are modeled by the detector simulation.

Cosmic rays are analyzed to identify stopping muons, spallation neutrons, and cosmogenic radioactive isotopes. Several thousand spallation neutrons per day are captured on hydrogen and gadolinium in the ID.

The use of the calibration data for issues of energy uniformity, stability, non-linearity and absolute calibration is described in Section IV E. The neutron detection efficiency from ^{252}Cf is described in Section V F. Good control of uncertainties on detection efficiency is essential for sensitivity to neutrino disappearance with a single detector. The detailed calibration data allow a precise energy-shape fit to the prompt neutrino candidates for the most sensitive extraction of θ_{13}.

III. REACTOR AND DETECTOR MODELS

A. Thermal Power

Double Chooz's sources of antineutrinos are the reactor cores B1 and B2 at the Électricité de France (EDF) Centrale Nucléaire de Chooz. Antineutrinos are produced in nuclear reactors by the β-decay of the fission products. Four main isotopes, ^{235}U, ^{239}Pu, ^{238}U, and ^{241}Pu, provide >99.7% of the fissions and antineutrinos.

Chooz B1 and B2 are N4 type pressurized water reactor (PWR) cores, and as such are two of the most powerful cores in the world with nominal thermal power outputs of 4.25 GW$_{th}$ each. The instantaneous thermal power of each reactor core P_{th}^R is provided by EDF as a fraction of the total power and is evaluated over time steps of <1 minute. The instantaneous thermal power is derived from the in-core instrumentation with the most important variable being the temperature of the water in the primary loop.

The in-core instrumentation calibration is tested weekly using the heat balance in the secondary loop, which is heated by the primary loop containing water heated by fissions. In the secondary loop, steam is generated to drive turbines. By using measurements of the heat flow in the secondary loop, the thermal power can be measured. This test is performed with the reactor running at full power. The uncertainty at lower power is therefore slightly larger. The in-core instrumentation is re-calibrated if it deviates by more than the uncertainty in the heat balance measurement.

Since the accuracy of the thermal power measurement determines the maximum power at which the core can operate, EDF has performed a detailed study of the uncertainty in this measurement [32–34]. The dominant uncertainty on the weekly heat balance at the secondary loops comes from the measurement of the water flow. At the nominal full power of 4250 MW the final uncertainty is 0.5% (1 σ C.L.). Since the amount of data taken with one or two cores at intermediate power is small, this uncertainty is used for the mean power of both cores. This is smaller than the typical uncertainty for PWRs of 0.7% [35] and reflects optimizations in the pipe geometry of the secondary loop, as well as great care taken to understand the sensor uncertainties, including full-scale test stands for the most critical sensors.

B. Mean Cross Section per Fission

The mean cross section per fission is effectively a spectrum averaged cross section. It is given by

$$\langle \sigma_f \rangle = \sum_k \alpha_k \langle \sigma_f \rangle_k = \sum_k \alpha_k \int_0^\infty dE\, S_k(E)\, \sigma_{IBD}(E) \tag{1}$$

where α_k is the fractional fission rate of the kth isotope ($k = {}^{235}$U, ^{239}Pu, ^{238}U, ^{241}Pu), $S_k(E)$ is the reference spectrum of the kth isotope and σ_{IBD} is the inverse beta decay cross section. The determinations of the α_k require the simulation of the reactor core (Section III C).

The antineutrino spectrum for each fission isotope is the result of the beta decays of many different fission products. For ^{235}U, ^{239}Pu, and ^{241}Pu, the reference antineutrino spectra are derived from measurements of the β spectra at the ILL research reactor [36–38]. In the case of ^{238}U, an ab initio calculation of the spectrum is used [39]. The conversion of the β spectra to antineutrino spectra has recently been improved by using more data on the many β transitions and higher order energy corrections [39, 40]. We use the conversion scheme of [40] including corrections for off-equilibrium effects[41]. The uncertainty on these spectra is energy dependent but is on the order of 3%. The new technique for the analysis of the β spectra has led to an overall change in the normalization of the $S_k(E)$ that, when applied to previous reactor antineutrino experiments, results in measurements that are lower than predictions for experiments at short baselines [41].

C. Fission Rate Computation

The fractional fission rates α_k of each isotope are needed in order to calculate the mean cross section per fission of (Equation 1). They are also required for the calculation of the mean energy released per fission for reactor R:

$$\langle E_f \rangle_R = \sum_k \alpha_k \langle E_f \rangle_k. \tag{2}$$

The mean energies released per fission per isotope $\langle E_f \rangle_k$ are summarized in Table I. The thermal power one would calculate given a fission is relatively insensitive to the specific fuel composition since the $\langle E_f \rangle_k$ differ by <6%; however, the difference in the detected number of antineutrinos is amplified by the dependence of the norm and mean energy of $S_k(\mathrm{E})$ on the fissioning isotope. For this reason, much effort has been expended in developing simulations of the reactor cores to accurately model the evolution of the α_k.

Double Chooz has chosen two complementary codes for modeling of the reactor cores: MURE and DRAGON [42–45]. MURE is a 3D full core simulation which uses Monte Carlo techniques to model the neutron transport in the core. DRAGON is a 2D simulation which models the individual fuel assemblies. Using some approximations, it solves the neutron transport equation in the core. These two codes provide the needed flexibility to extract fission rates and their uncertainties. These codes were benchmarked against data from the Takahama-3 reactor and were found to be consistent other codes commonly used in the reactor industry for reactor modeling within the uncertainty in the Takahama data [46].

The construction of the reactor model requires detailed information on the geometry and materials comprising the core. The Chooz cores are comprised of 205 fuel assemblies. For every reactor fuel cycle, approximately one year in duration, one third of the assemblies are replaced with assemblies containing fresh fuel. The other two thirds of the assemblies are redistributed to obtain a homogeneous neutron flux across the core. The Chooz reactor cores contain four assembly types that differ mainly in their initial ^{235}U enrichment. These enrichments are 1.8%, 3.4% and 4%.

The data set presented here spans fuel cycle 12 for core B2 and cycle 12 and the beginning of cycle 13 for B1. EDF provides Double Chooz with the locations and initial burnup of each assembly. Based on these maps, a full core simulation was constructed using MURE for each cycle. In addition, the beginning-of-fuel-cycle composition needs to be determined based on the burnup of each assembly. To accomplish this, an assembly-level reference simulation is run using both MURE and DRAGON for each of the four fuel assembly types. The results of the reference simulations are compared to EDF's own simulation code APOLLO2-F from which the burnup values are derived. The uncertainty due to the simulation technique is evaluated by comparing the DRAGON and MURE results for the reference simulation leading to a small 0.2% systematic uncertainty in the fission rate fractions α_k.

Once the initial fuel composition of the assemblies is known, MURE is used to model the evolution of the full core in time steps of 6 to 48 hours, depending on the operating conditions of the reactor. The results from each simulation time step are written to a database. This allows the α_k's, and therefore the predicted antineutrino flux, to be calculated. The results averaged over the current data set are shown in Table I.

The systematic uncertainties on the α_k's are determined by varying the inputs and observing their effect on the fission rate relative to the nominal simulation. The uncertainties considered are those due to the thermal power, boron concentration, moderator temperature and density, initial burnup error, control rod positions, choice of nuclear databases, choice of the energies released per fission, and statistical error of the MURE Monte Carlo. The systematic errors associated with each input are considered independently and the uncertainties propagated quadratically. The correlation coefficients among isotopic fission rates due to the thermal power constraint are also computed, and a covariance matrix is constructed with these contributions in order to properly account for those

TABLE I. Mean energy released per fission $\langle E_f \rangle_k$ from [47] and fractional fission rate $\langle \alpha_k \rangle$ of the isotope k for this data.

Isotope	$\langle E_f \rangle_k$ (MeV)	$\langle \alpha_k \rangle$
^{235}U	201.92±0.46	0.496±0.016
^{239}Pu	209.99±0.60	0.351±0.013
^{238}U	205.52±0.96	0.087±0.006
^{241}Pu	213.60±0.65	0.066±0.007

correlations. The uncertainties in the α_k's are listed in Table I. The two largest contributions come from the moderator density and control rod positions.

D. Bugey4 Normalization and Antineutrino Rate Calculation

In the current, far-only, phase of Double Chooz, the rather large uncertainties in the reference spectra of Section III B limited our sensitivity to θ_{13}. To mitigate this effect, the normalization of the cross section per fission for each reactor is "anchored" to the Bugey4 rate measurement at 15 m [48]:

$$\langle \sigma_f \rangle_R = \langle \sigma_f \rangle^{Bugey} + \sum_k (\alpha_k^R - \alpha_k^{Bugey})\langle \sigma_f \rangle_k. \quad (3)$$

where R stands for each reactor. The second term corrects for the difference in fuel composition between Bugey4 and each of the Chooz cores. This treatment takes advantage of the high accuracy of the Bugey4 anchor point (1.4%) and suppresses the dependence on the predicted $\langle \sigma_f \rangle_R$. This is due to the smallness of the correction term $(\alpha_k^R - \alpha_k^{Bugey})$. At the same time, the analysis becomes insensitive to possible oscillations at shorter baselines due to heavy $\Delta m^2 \sim 1~eV^2$ sterile neutrinos.

The expected number of antineutrinos with no oscillation in the ith energy bin with the Bugey4 anchor point becomes:

$$N_i^{exp,R} = \frac{\epsilon N_p}{4\pi} \frac{1}{L_R^2} \frac{P_{th}^R}{\langle E_f \rangle_R}$$
$$\times \left(\frac{\langle \sigma_f \rangle_R}{(\sum_k \alpha_k^R \langle \sigma_f \rangle_k)} \sum_k \alpha_k^R \langle \sigma_f \rangle_k^i \right) \quad (4)$$

where ϵ is the detection efficiency, N_p is the number of protons in the target, L_R is the distance to the center of each reactor, and P_{th}^R is the thermal power. The variable $\langle E_f \rangle_R$ is the mean energy released per fission defined in Equation 2, while $\langle \sigma_f \rangle_R$ is the mean cross section per fission defined in Equation 3. The three variables P_{th}^R, $\langle E_f \rangle_R$ and $\langle \sigma_f \rangle_R$ are time dependent with $\langle E_f \rangle_R$ and $\langle \sigma_f \rangle_R$ depending on the evolution of the fuel composition in the reactor and P_{th}^R depending on the operation of the reactor.

A covariance matrix $M_{ij}^{exp} = \delta N_i^{exp} \delta N_j^{exp}$ is constructed using the uncertainties listed in Table II. This

TABLE II. The uncertainties in the antineutrino prediction. All uncertainties are assumed to be correlated between the two reactor cores. They are assumed to be normalization and energy (rate and shape) unless noted as normalization only.

Source	Normalization Only	Uncertainty [%]
P_{th}	yes	0.5
$\langle \sigma_f \rangle^{Bugey}$	yes	1.4
$S_k(E)\sigma_{IBD}(E_\nu^{true})$	no	0.2
$\langle E_f \rangle$	no	0.2
L_R	yes	<0.1
α_k^R	no	0.9
Total		1.8

matrix is constructed in terms of real energy and is converted into reconstructed energy by running multiple simulations drawn from a Cholesky decomposition of M_{ij}^{exp}. For these simulations, the full detector Monte Carlo described below is used. The use of Equation 4 to construct the covariance matrix allows time and spectral information to propagate to the final analysis.

The IBD cross section used is the simplified form from Vogel and Beacom [49] :

$$\sigma_{IBD}(E_\nu^{true}) = E_{e+}K\sqrt{E_{e+}^2 - m_e^2} \quad (5)$$

where

$$E_{e+} = \frac{1}{2}\left(\sqrt{m_n^2 - 4m_p\left(-E_\nu + \Delta + \frac{\Delta^2 - m_e^2}{2m_p}\right)} - m_n \right) \quad (6)$$

and m_e and E_{e+} are the positron mass and energy. The variables m_n and m_p are the masses of the neutron and proton with $\Delta = m_n - m_p$. The constant K is inversely proportional to the neutron lifetime. We use the MAMBO-II measurement of the neutron lifetime [50] and find $K = 0.961 \times 10^{-43}$ cm^2 MeV^{-2}.

E. Detector Model

We model the detector response using a detailed Geant4 [51] simulation with enhancements to the scintillation process, photocathode optical surface model, and thermal neutron model. Apart from these additions, the physics list is similar to Geant4's `QGSP_BERT_HP` reference physics list [52], without processes for high-mass hadrons. Our custom scintillation process implements detailed light waveforms, spectra, re-emission, and Birkslaw [53] quenching. Our photocathode model is based on a standard mathematical model of a thin, semitransparent surface with absorption and refractive index [54], and also includes the collection efficiency for photoelectrons as a function of position of emission on the photocathode. Our custom neutron thermalization process implements molecular elastic scattering for neutrons under 4 eV and a

radiative capture model with improved final state gamma modeling.

The simulation models the detector geometry to a fine level of detail, particularly with regard to the geometry of the phototubes and mu-metal shields and of all materials near the active volume such as tank walls and supports. The orientation and positions of the phototube assemblies were set using data from a photographic survey with sub-mm accuracy. The dimensions of the tank walls and supports were checked by experimenters during assembly and installation, and placement also verified by photographic survey.

Simulated IBD events are generated with run-by-run correspondence of MC to data, with fluxes and rates calculated as described in Section III D. Radioactive decays in calibration sources and spallation products were simulated using detailed models of nuclear levels, taking into account branching ratios and correct spectra for transitions [55].

Optical parameters used in the detector model are based on detailed measurements made by the collaboration. The relative light yield of the NT compared to the GC was measured using a Compton backscatter peak method in order to select scattered electrons with fixed energy [21]. Tuning of the absolute and relative light yield in the simulation was done with calibration data. The scintillator emission spectrum was measured using a Cary Eclipse fluorometer [56]. The photon emission time probabilities used in the simulation are obtained with a dedicated laboratory setup [16]. For the ionization quenching treatment in our MC, the light output of the scintillators after excitation by electrons [57] and alpha particles [58] of different energies was measured. The non-linearity in light production in the simulation has been adjusted to match these data. The attenuation and re-emission probabilities of each of the scintillator components in the relevant wavelength range are implemented in the MC. The fine-tuning of the total attenuation was made using measurements of the complete scintillators [16]. Other measured optical properties include reflectivities of various detector surfaces and indices of refraction of detector materials.

F. Readout System Simulation

The Readout System Simulation (RoSS) accounts for the response of elements associated with detector readout, such as from the PMTs, FEE, FADCs, trigger system and DAQ. The simulation relies on the measured probability distribution function (PDF) to empirically characterize the response to each single PE as measured by the full readout channel. The Geant4-based simulation calculates the time at which each PE strikes the photocathode of each PMT. RoSS converts this time-per-PE into an equivalent waveform as digitized by FADCs. A dedicated setup was built to measure most of the necessary PDFs as well as to tune the design of the full

readout chain. Channel-to-channel variations, such as gains, baselines, noise, single PE widths, etc., are taken into consideration, to accurately predict dispersion effects. This capability allows the simulation to exhibit non-linearity effects as observed in the data, as described in Section II F. After calibration, the MC and data energies agree within 1%. About 25% of the width of the calibrated H-capture (2.2 MeV γ line) results from readout effects; i.e., effects beyond photon-statistics fluctuations.

G. Monte Carlo $\bar{\nu}_e$ Event Generation

A set of Monte Carlo $\bar{\nu}_e$ events representing the expected signal for the duration of physics data-taking is created based on the formalism of Equation 4. The calculated IBD rate is used to determine the rate of interactions. Parent fuel nuclide and neutrino energies are sampled from the calculated neutrino production ratios and corresponding spectra, yielding a properly normalized set of IBD-progenitor neutrinos.

Once generated, each event-progenitor neutrino is assigned a random creation point within the originating reactor core. The event is assigned a weighted-random interaction point within the detector based on proton density maps of the detector materials. In the center-of-mass frame of the $\nu - p$ interaction, a random positron direction is chosen, with the positron and neutron of the IBD event given appropriate momenta based on the neutrino energy and decay kinematics. These kinematic values are then boosted into the laboratory frame. The resulting positron and neutron momenta and originating vertex are then available as inputs to the Geant4 detector simulation. "Truth" information regarding the neutrino origin, baseline, and energy are propagated along with the event, for use later in the oscillation analysis.

IV. RECONSTRUCTION

A. Pulse Reconstruction

The pulse reconstruction provides the signal charge and time in each PMT. Pulser triggers are taken with a rate of 1 Hz in order to provide accurate information about the baseline for each of the 468 readout channels. The baseline mean (B_{mean}) and rms (B_{rms}) are computed using the full readout window (256 ns).

The integrated charge (q) is defined as the sum of digital counts in each waveform sample over the integration window, once the pedestal has been subtracted. The pedestal is computed as the integration of B_{mean} over the same window. In order to improve the charge resolution, the size of the integral window has been set to a 112 ns subsample of the readout one, based on the width of the single PE signals.

In order to find the pulses within the readout window, a dynamic window algorithm is used. The algo-

rithm searches for the 112 ns window which maximizes the integral. In the absence of an actual PE signal, this algorithm would reconstruct the largest noise fluctuation, leading to a bias in the charge reconstruction. To address this, we introduce two requirements: ≥ 2 ADC counts in the maximum bin, and $q > B_{rms} \times \sqrt{N_s}$, where N_s is the number of integrated waveform samples (56 for a 112 ns window). For each pulse reconstructed, the start time is computed as the time when the pulse reaches 20% of its maximum. This time is then corrected by the PMT-to-PMT offsets obtained with the LI system.

B. Vertex Reconstruction

Vertex reconstruction in Double Chooz is not used for event selection, but is used for event energy reconstruction. It is based on a maximum charge and time likelihood algorithm which utilizes all hit and no-hit information in the detector. Assuming the event to be a point-like source of light characterized by the set

$$\mathbf{X} = (x_0, y_0, z_0, t_0, \Phi) \qquad (7)$$

where (x_0, y_0, z_0) is the event position in the detector, t_0 is the event time and Φ is the light intensity per unit solid angle (expressed in photons/sr), the amount of light and prompt arrival time at the i-th PMT can be predicted as

$$\mu_i = \Phi \, \epsilon_i \, \Omega_i \, A_i \qquad (8)$$

and

$$t_i^{(pred)} = t_0 + \frac{r_i}{c_n} \qquad (9)$$

respectively, where ϵ_i is the quantum efficiency of the PMT, Ω_i is the solid angle subtended by the PMT at a distance r_i from the event vertex, A_i is the light transmission amplitude, and c_n is the effective speed of light in the medium.

The event likelihood is defined as

$$\mathcal{L}(\mathbf{X}) = \prod_{q_i=0} f_q(0; \mu_i) \prod_{q_i>0} f_q(q_i; \mu_i) f_t(t_i; t_i^{(pred)}, \mu_i) \quad (10)$$

where the first product goes over the PMTs that have not been hit, while the second product goes over the remaining PMTs that have been hit (i.e., have a non-zero recorded charge q_i at the registered time t_i). $f_q(q_i; \mu_i)$ is the probability to measure a charge q_i given an expected charge μ_i, and $f_t(t_i; t_i^{(pred)}, \mu_i)$ is the probability to measure a time t_i given a prompt arrival time t_i^{pred} and predicted charge μ_i. These are obtained from MC simulations and verified against the physics and calibration data. The task of the event reconstruction is to find the best possible set of event parameters $\mathbf{X}_{min}$ which maximizes the event likelihood $\mathcal{L}(\mathbf{X})$, or equivalently, minimizes the negative log-likelihood function

$$F(\mathbf{X}) = -\ln \mathcal{L}(\mathbf{X}) = -\sum_i \ln f_q(q_i; \mathbf{X})$$

$$-\sum_{q_i>0} \ln f_t(t_i; \mathbf{X}) = F_q(\mathbf{X}) + F_t(\mathbf{X}). \qquad (11)$$

Note that the event reconstruction can be performed using either one or both of the two terms in the expression above, F_q for a charge-only reconstruction, or F_t for a time-only reconstruction; utilizing both components enhances the accuracy and stability of the algorithm.

The performance of the Double Chooz reconstruction has been evaluated in situ using radioactive sources deployed at known positions along the z-axis in the target volume, and off-axis in the guide tubes. The sources are reconstructed with a spatial resolution of 32 cm for ^{137}Cs, 24 cm for ^{60}Co, and 22 cm for ^{68}Ge.

C. Muon tagging and reconstruction

Cosmic muons passing through the detector or the nearby rock induce backgrounds which are discussed in the next section. A through-going (stopping) muon typically deposits 160 MeV (80 MeV) in the IV which triggers above about 10 MeV. The IV trigger rate is 46 s^{-1}. All muons in the ID are tagged by the IV except some stopping muons which enter the chimney. Muons which stop in the ID and their resulting Michel e can be identified by demanding a large energy deposition (roughly a few tens of MeV) in the ID. An event is tagged as a muon if there is > 5 MeV in the IV or > 30 MeV in the ID.

Several tracking algorithms have been developed to reconstruct these muons. IV reconstruction is based on a maximum likelihood algorithm utilizing the arrival times of the earliest photons to hit each PMT, while ID reconstruction utilizes the spatial pattern of hit times. The forward wavefront of scintillation light from a relativistic track propagates at the Cerenkov angle, thus allowing the same algorithm to be used for tracks in the NT, GC, and non-scintillating buffer. Using MC and the OV as reference, the lateral resolution at the detector center has been determined to be 35 cm for ID and 60 cm for IV muons.

D. Light Noise Rejection

The background known as *light noise* is caused by a sporadic spontaneous flashes of some PMT bases. The characteristic signature is light mainly localized to one PMT base and spread out in time among the other PMTs after many reflections from the detector surfaces. This background can be discriminated from physics events based on the fact that the detected light is spread less homogeneously across the detector for light noise events. Light noise is rejected by demanding both a small value of

Q_{max}/Q_{tot}, where Q_{max} is the maximum charge recorded by a single PMT and Q_{tot} is the total ID charge collected in a trigger, and large values of $rms(t_{start})$, which is the standard deviation of the distribution of the start time (t_{start}) of the first pulse on each PMT.

E. Energy Reconstruction

The visible energy (E_{vis}) provides the absolute calorimetric estimation of the energy deposited per trigger. E_{vis} is a function of the calibrated PE (total number of photoelectrons):

$$E_{vis} = PE^m(\rho, z, t) \times f_u^m(\rho, z) \times f_s^m(t) \times f_{MeV}^m, \quad (12)$$

where $PE = \sum_i pe_i = \sum_i q_i/gain_i(q_i)$. Coordinates in the detector are ρ and z, t is time, m refers to data or Monte Carlo (MC) and i refers to each good channel. The correction factors f_u, f_s and f_{MeV} correspond, respectively, to the spatial uniformity, time stability and PE/MeV calibrations. Four stages of calibration are carried out to render E_{vis} linear, independent of time and position, and consistent between data and MC. Both the MC and data are subjected to the same stages of calibration.

The sum over all good channels of the reconstructed raw charge (q_i, see Section IV A) from the digitized waveforms is the basis of the energy estimation. Good channels are those identified and tagged as well behaved by fast online analysis based on waveform information. Only a very few channels are sporadically not good and are, thus, excluded from the calorimetric estimation. The limited sampling of the waveform baseline estimation can be biased [28] leading to a non-linearity at about 1 PE charge equivalent. Figure 4 shows the effect for a representative channel. A similar curve is used to calibrate the MC. The PE calibrated charge (pe_i) is defined as $pe_i = q_i/gain_i(q_i)$. One $gain_i(q_i)$ curve is generated upon each power-cycle episode. Due to the average light level ($\sim 230\ PE$/MeV), the non-linear bias of the single-PE calibration can have up to a 10% effect for energies below 3 MeV, if not corrected.

The PE response is position dependent for both MC and data. Calibration maps were created such that any PE response for any event located at any position (ρ,z) can be converted into its response as if measured at the center of the detector ($\rho = 0, z = 0$): $PE_\odot^m = PE^m(\rho, z) \times f_u^m(\rho, z)$. The calibration map's correction for each point is labeled $f_u^m(\rho, z)$. Independent uniformity calibration maps $f_u^m(\rho, z)$ are created for data and MC, such that the uniformity calibration serves to minimize any possible difference in position dependence of the data with respect to MC. The capture peak on H (2.223 MeV) of neutrons from spallation and antineutrino interactions provides a precise and copious calibration source to characterize the response non-uniformity over the full volume (both NT and GC). The calibration map for data is shown in Figure 5. A similar map
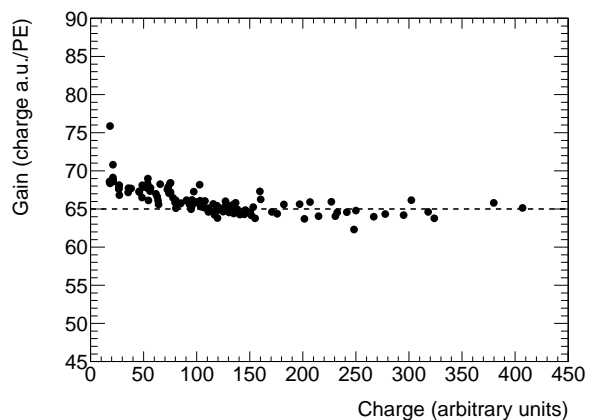

FIG. 4. Demonstration of the linear PE calibration for one channel. The gain versus charge is shown. The dashed line highlights the constant component (linear behavior) of the gain observed at large charges. The calibration parametrizes this curve to correct the non-linear component (deviation from constant) of the gain, making the PE corrected energy scale linear to within 2%.
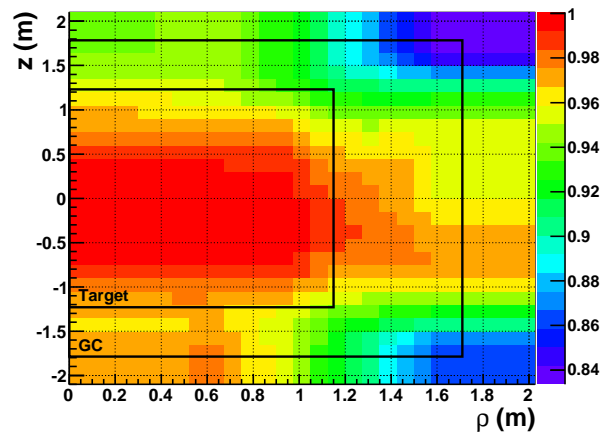

FIG. 5. Detector calibration map, in cylindrical coordinates (ρ,z), as sampled with spallation neutrons capturing in H across the ID. Response variations are quantified as the fractional response with respect to the detector center. Largest deviation in NT are up to 5%. A similar map is constructed with MC for calibration of its slightly different response uniformity pattern.

was measured and applied to MC. A 2D-interpolation method was developed to provide a smooth application of the calibration map at any point (ρ, z).

The detector response stability was found to vary in time due to two effects, which are accounted for and corrected by the term $f_s^m(t)$. First, the detector response can change due to variations in readout gain or scintillator response. This effect has been measured as a +2.2% monotonic increase over 1 year using the response of the spallation neutrons capturing on Gd within the NT, shown in Figure 2. Second, a few readout chan-
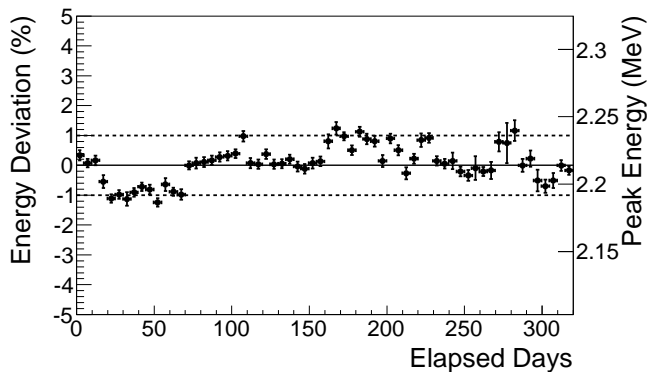
FIG. 6. Stability of the reconstructed energy as sampled by the evolution in response of the spallation neutron H-capture after stability calibration. The observed steps correspond to power-cycle periods. The systematic uncertainty on the energy stability is estimated at 0.61%.

TABLE III. Energy scale systematic errors.

	Error (%)
Relative Non-Uniformity	0.43
Relative Instability	0.61
Relative Non-Linearity	0.85
Total	1.13

nels varying over time are excluded from the calorimetry sum, and the average overall response decreases by 0.3% per channel excluded. The MC is stable, so this correction is applied only to data. The stability calibration is relative to a specific reference time t_0. Therefore, any response $PE_\odot(t)$ is converted to the equivalent response at t_0, as $PE^m_{\odot t_0} = PE^m_\odot(t) \times f^m_s(t)$. The t_0 was defined as the day of the first Cf source deployment, during August 2011. The remaining instability after calibration is shown in Figure 6, as sampled with H-capture from spallation neutrons, and is used for the stability systematic uncertainty estimation.

The number $PE_{\odot t_0}$ per MeV is determined by an absolute energy calibration independently, for the data and MC. The response in $PE_{\odot t_0}$ for H-capture as deployed in the center of the NT is used for the absolute energy scale. The absolute energy scales are found to be 229.9 $PE_{\odot t_0}$/MeV and 227.7 $PE_{\odot t_0}$/MeV, respectively, for the data and MC, demonstrating agreement within 1% prior to this calibration stage.

Discrepancies in response between the MC and data, after calibration, are used to estimate these uncertainties within the prompt energy range and the NT volume. Table III summarizes the systematic uncertainty in terms of the remaining non-uniformity, instability and non-linearity. The relative non-uniformity systematic uncertainty was estimated from the calibration maps using neutrons capturing on Gd, after full calibration. The rms deviation of the relative difference between the data and MC calibration maps is used as the estimator of

the non-uniformity systematic uncertainty, and is 0.43%. This result is consistent with the analysis of all calibration sources along the z-axis (NT) and GT (GC). The relative instability systematic error, discussed above, is 0.61%. Responses are equalized at 2.223 MeV, but small data/MC discrepancies in the absolute energy scale can still arise from the relative non-linearity across the prompt energy spectrum. This possibility was explored by using all calibration sources in the energy range 0.7 – 8 MeV with deployments along the z-axis and GT. Some relative non-linearity was observed ($< 0.2\%$/MeV) but the pattern diminished when integrated over the full volume. A 0.85% variation consistent with this non-linearity was measured with the z-axis calibration system, and this is used as the systematic error for relative non-linearity in Table III. Consistent results were obtained when sampling with the same sources along the GT.

V. NEUTRINO DATA ANALYSIS

A. $\bar{\nu}_e$ Candidate Selection

The $\bar{\nu}_e$ candidate selection procedure starts in a similar way as [7]. Events with an energy below 0.5 MeV, where the trigger efficiency is not 100%, or identified as light noise ($Q_{max}/Q_{tot} > 0.09$ or $\text{rms}(t_{start}) > 40$ ns) are discarded. Triggers within a 1 ms window following a tagged muon are also rejected (see Section IV C), in order to reduce the correlated and cosmogenic backgrounds. The effective veto time is 4.4% of the total run time. Defining $\Delta T \equiv t_{delayed} - t_{prompt}$, further selection consists of 4 cuts:

1. time difference between consecutive triggers (prompt and delayed): $2\ \mu s < \Delta T < 100\ \mu s$, as shown in Figure 7, where the lower cut reduces correlated backgrounds and the upper cut is determined by the approximately 30 μs capture time on Gd;

2. prompt trigger: $0.7\ \text{MeV} < E_{prompt} < 12.2\ \text{MeV}$, as illustrated in Figure 8;

3. delayed trigger: $6.0\ \text{MeV} < E_{delayed} < 12.0\ \text{MeV}$ (Figure 8) and $Q_{max}/Q_{tot} < 0.055$;

4. multiplicity: no additional triggers from 100 μs preceding the prompt signal to 400 μs after it, with the goal of reducing the correlated background.

The IBD efficiencies for these cuts are listed in Table IV.

A preliminary sample of 9021 candidates is obtained by applying selections (1–4). In order to reduce the background contamination in the sample, candidates are rejected according to two extra cuts not used in [7]. First, candidates within a 0.5 s window after a high energy muon crossing the ID ($E_\mu > 600$ MeV) are tagged as cosmogenic isotope events and rejected, increasing the

Cut	Efficiency %
E_{prompt}	100.0 ± 0.0
E_{delayed}	94.1 ± 0.6
ΔT	96.2 ± 0.5
Multiplicity	99.5 ± 0.0
Muon veto	90.8 ± 0.0
Outer Veto	99.9 ± 0.0

TABLE IV. Cuts used in the event selection and their efficiency for IBD events. The OV was working for the last 68.9% of the data.
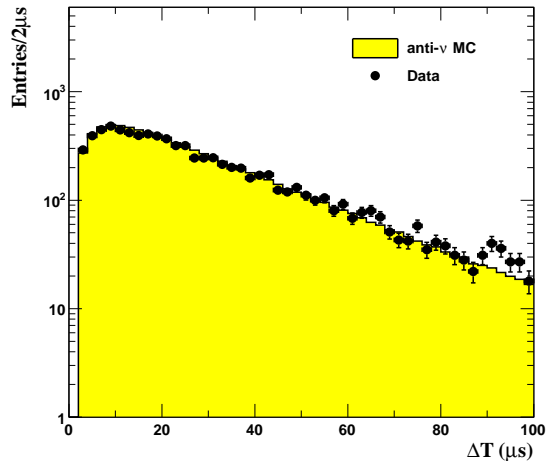

FIG. 7. Time difference between prompt and delayed triggers. Black dots and solid histogram show data and MC results, respectively.

FIG. 8. Delayed energy versus prompt energy for time-correlated triggers. Vertical and horizontal dashed lines show the cuts applied for $\bar{\nu}_e$ candidates selection.

effective veto time to 9.2%. Second, candidates whose prompt signal is coincident with an OV trigger are also excluded as correlated background. Applying the above vetoes yields 8249 candidates or a rate of 36.2 ± 0.4 events/day, uniformly distributed within the target, for an analysis livetime of 227.93 days. This rate is lower than the one presented in [7] due to a longer data taking period with one reactor being off, as well as to the new cuts reducing the background contamination. Following the same selection procedure on the $\bar{\nu}_e$ MC sample yields 8439.6 expected events in the absence of oscillation.

B. Accidental Background

The main source of accidental coincidences is the random association of a prompt trigger from natural radioactivity and a later neutron-like candidate. This background is estimated by applying the neutrino selection cuts described in Section V A but using coincidence windows shifted by 1 s in order to remove correlations in the time scale of n-captures in H and Gd. The statistics of

the sample is enhanced by using 198 windows each shifted from the previous one by 500 μs. The radioactivity rate between 0.7 and 12.2 MeV is 8.2 s^{-1}, while the singles rate in 6 - 12 MeV energy region is 18 h^{-1}. Both rates are quite stable along the data taking period. Finally, the accidental background rate is found to be 0.261 ± 0.002 events per day. The reproducibility of our result and any possible systematic effect are studied by repeating the procedure 30 times, i.e., taking 30 times 198 consecutive time windows. The dispersion of these 30 measurements is consistent with only statistical error, so, no systematic deviation is found.

Figure 9 shows the accidental prompt spectrum and the energy distribution for natural radioactivity scaled to the number of accidental events; the agreement is excellent. The distribution is peaked at low energies below 3 MeV. The remaining light noise is included in the accidental background sample. Using the correlation between both variables $Q_{\text{max}}/Q_{\text{tot}}$ and rms(t_{start}), its contribution to the accidental sample is estimated to be lower than 1%.

C. Cosmogenic Isotopes Background

The radioisotopes ^{8}He and ^{9}Li are products of spallation processes on ^{12}C induced by cosmic muons crossing the scintillator volume. The βn-decays of these isotopes constitute a background for the antineutrino search. βn-emitters can be identified from the time- and space- correlation to their parent muon. Due to their relatively long lifetimes (^{9}Li: $\tau = 257$ ms, ^{8}He: $\tau = 172$ ms), an event-by-event discrimination is not possible. For the
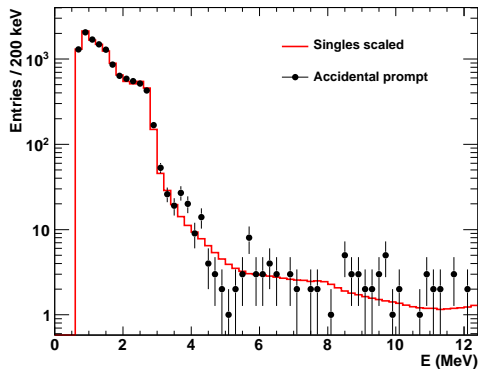
FIG. 9. The accidental prompt spectrum (black circles) superimposed to the radioactivity energy distribution measured in Double Chooz scaled to the same number of entries (red line).

FIG. 10. The prompt β spectrum of the βn-emitters ^{8}He and ^{9}Li from data (black squares) and Monte Carlo (red line), assuming ^{9}Li is the dominant contribution.

muon rates in our detector, vetoing for several isotope lifetimes after each muon would lead to an unacceptably large loss in exposure. Instead, the rate is determined by an exponential fit to the $\Delta t_{\mu\nu} \equiv t_\mu - t_\nu$ profile of all possible muon-IBD candidate-pairs.

The analysis is performed for three visible energy E_μ^{vis} ranges that characterize subsamples of parent muons by their energy deposition, not corrected for energy non-linearities, in the ID:

1. Showering muons crossing the target value are selected by $E_\mu^{vis} > 600\,\text{MeV}$ and feature an increased probability to produce cosmogenic isotopes. The $\Delta t_{\mu\nu}$-fit returns a precise result of 0.95 ± 0.11 events/day for the βn-emitter rate.

2. In the E_μ^{vis} range from 275 to 600 MeV, muons crossing GC and target still give a sizable contribution to isotope production of 1.08 ± 0.44 events/day. To obtain this result from a $\Delta t_{\mu\nu}$ fit, the sample of muon-IBD pairs has to be cleaned by a spatial cut on the distance of closest approach from the muon to the IBD candidate of $d_{\mu\nu} < 80\,\text{cm}$ to remove the majority of uncorrelated pairs. The corresponding cut efficiency is determined from the lateral distance profile obtained for $E_\mu^{vis} > 600\,\text{MeV}$. The approach is validated by a comparative study of cosmic neutrons that show an almost congruent profile with very little dependence on E_μ^{vis} above 275 MeV.

3. The Cut $E_\mu^{vis} < 275\,\text{MeV}$ selects muons crossing only the buffer volume or the rim of the GC. For this sample, no production of βn-emitters inside the target volume is observed. An upper limit of < 0.3 events/day can be established based on a $\Delta t_{\mu\nu}$ fit for $d_{\mu\nu} < 80\,\text{cm}$. Again, the lateral distribution of cosmic neutrons has been used for determining the cut efficiency.
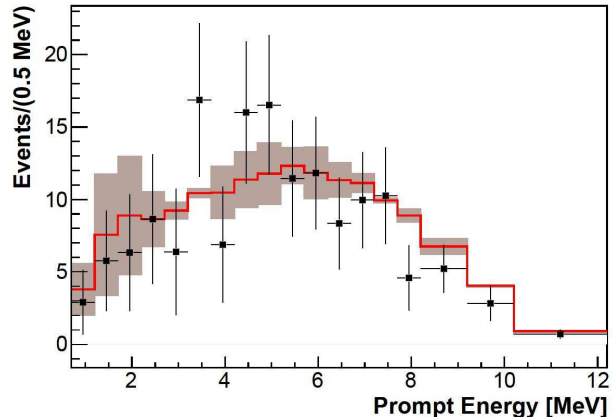
The overall rate of βn-decays found is $2.05^{+0.62}_{-0.52}$ events/day. The result of a similar analysis based on the IV muon tracking agrees within the uncertainty.

Accidental coincidences containing the β-decay of the isotope ^{12}B either as prompt or as delayed event feature a time correlation to the parent muons producing the ^{12}B. In the $\Delta t_{\mu\nu}$ profile, these events are represented by a decay function with $\tau(^{12}B) = 29\,\text{ms}$. However, these events were removed very efficiently from the data set used for ^{9}Li analysis by imposing a maximum distance cut of 90 cm between prompt and delayed events, introducing a negligible inefficiency of $\sim 1\%$.

The correlation of a cosmogenic isotope to the showering muons has been exploited to impose a partial veto of this background for the final fit analysis. Vetoing all IBD candidates within 0.5 s following a muon of $E_\mu^{vis} > 600\,\text{MeV}$, 0.89 ± 0.10 events d^{-1} of βn-decays are removed from the data sample. The residual cosmogenic isotope background rate has been determined to 1.25 ± 0.54 events/day.

Finally, the correlation of parent muons and βn-emitters has been used to extract the prompt β spectrum from the data. Figure 10 shows a sample spectrum obtained for $E_\mu > 620\,\text{MeV}$, a distance cut of 0.7 m and a $\Delta t_{\mu\nu}$ cut of 600 ms. The contamination of the sample by random coincidences has been statistically subtracted. Good agreement is found for the MC spectrum used in the final fit analysis.

D. Fast Neutrons and Stopping Muon Background

Most correlated backgrounds are rejected by the 1 ms veto time after each tagged muon. The remaining events arise from cosmogenic events whose parent muon either misses the detector or deposits an energy low enough to escape the muon tagging. Two contributions have been found: fast neutrons (FN) and stopping muons (SM).

FN are created by muons in the inactive regions surrounding the detector. Their large interaction length allows them to cross the detector and capture in the ID, causing both a prompt trigger by recoil protons and a delayed trigger by capture on Gd. An approximately flat prompt energy spectrum is expected; a slope could be introduced by acceptance and scintillator quenching effects. The time and spatial correlation distribution of FN are indistinguishable from those of $\bar{\nu}_e$ events.

The selected SM arise from muons entering through the chimney, stopping in the top of the ID, and eventually decaying. The short muon track mimics the prompt event, and the decay Michel electron mimics the delayed event. SM candidates are localized in space in the top of the ID under the chimney, and have a prompt-delayed time distribution following the 2.2 μs muon lifetime.

The correlated background has been studied by extending the selection on E_{prompt} up to 30 MeV. No IBD events are expected in the interval 12 MeV $\leq E_{\text{prompt}} \leq$ 30 MeV. FN and SM candidates were separated via their different correlation time distributions. A $97^{+3}_{-8}\%$ pure sample of FN is obtained for $\Delta T > 10$ μs, and a $(88\pm7)\%$ pure sample of SM is obtained for $\Delta T < 10$ μs. These samples of FN and SM can be used to estimate their rate. The observed prompt energy spectrum is consistent with a flat continuum between 12 and 30 MeV, which extrapolated to the IBD selection window provides a first estimation of the correlated background rate of ≈ 0.75 events/day. The accuracy of this estimate depends on the validity of the extrapolation of the spectral shape. Next we describe a measurement of the FN and SM spectral shapes including the IBD region, obtained by using the IV and OV to tag samples of FN and SM.

The DAQ reads out the IV upon any ID trigger, lowering the IV detection threshold to ~ 1 MeV, and making the IV sensitive to FN via the detection of proton recoils and captures on H. The IV-tagging is implemented by demanding at least 2 IV PMT hits leading to $(33 \pm 5)\%$ tagging efficiency with no contribution by single PMT energy depositions. There is a very low probability of accidental IV tagging due to any IV energy deposition in the 256 ns coincident readout window.

The OV-tagging, when available, is especially sensitive to SMs since the muon is often detected. $(41 \pm 23)\%$ of the FN and SM candidates in the 12-to-30-MeV window are tagged by the OV, of which $(74 \pm 12)\%$ are SM. OV-tagging has an accidental rate = 0.06% of the neutrino sample and can be used to veto events caused by muons.

Several FN and SM analyses were performed using different combinations of IV and OV tagging. The main analysis for the FN estimation relies on IV-tagging of the prompt triggers with OV veto applied for the IBD selection. Two sources of backgrounds on the tagged FN sample were identified and rejected. The first source is the combination of natural radioactivity in the IV in an accidental coincidence with a genuine IBD, and was reduced to 12% by imposing a time coincidence between the ID and IV energy depositions. The second source, a Comp-
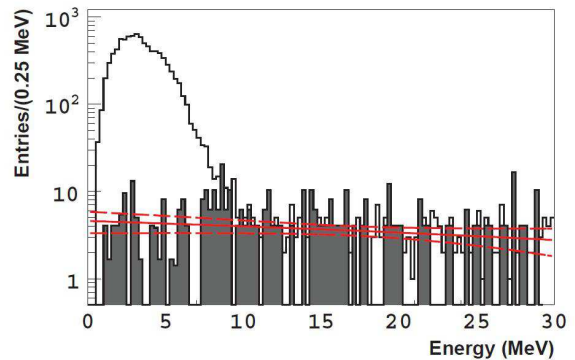

FIG. 11. FN and SM combined spectral model best fit (solid red) with $\pm 1\sigma$ (dashed red), energy distribution of tagged FN and SM population (gray histogram) and IBD spectrum.

ton scattering in both the IV and ID in an accidental coincidence with a Gd-capture, was reduced to 2% by imposing a cut on the spatial distance between the prompt and delayed candidate in the ID. The purity of the IV-tagged FN sample was 86%. The remaining background was measured in an off-time window and subtracted, thus minimizing distortions to the energy spectrum. The FN spectral shape was found to be in agreement with a linear model with a small positive slope. The measured total FN rate was (0.30 ± 0.14) events/day, including systematic uncertainties from the ΔT-based FN-SM separation, the IV-tagging efficiency, and background subtractions.

Since there is no correlation between the SM prompt energy and the delayed energy deposit of the Michel electron, a pure sample of SM was obtained by selecting 20 MeV $\leq E_{\text{delayed}} \leq$ 60 MeV. The spectral shape of SM prompt energy was found to be in agreement with a linear model with a small negative slope. The total SM rate was measured to be (0.34 ± 0.18) events/day, including systematic uncertainties.

Since the spectral shapes for both FN and SM are linear, a combined analysis was performed to obtain the total spectrum shown in Fig. 11 and the total rate estimation (0.67 ± 0.20) events/day summarized in Table V. Consistent results were obtained from different analysis techniques, which included IV- and OV-tagging without OV-vetoing. The OV veto reduces the rate of correlated backgrounds by about 30%.

E. Background Measurements

There are four ways that can be utilized to estimate backgrounds. Each independent background component can be measured by isolating samples and subtracting possible correlations. This is described for each component in Sections IV D, V C and V D. Second, we can measure each independent background component including spectral information when fitting for θ_{13} oscillations as is done in Section VI. Third, the total background rate is

measured by comparing the observed and expected rates as a function of reactor power. Fourth, we can use the both-reactor-off data to measure both the rate and spectrum.

The latter two methods are used currently as cross-checks for the background measurements due to low statistics and are described here. The measured daily rate of IBD candidates as a function of the no-oscillation expected rate for different reactor power conditions is shown in Figure 12. The extrapolation to zero reactor power of the fit to the data yields 2.9 ± 1.1 events per day, in excellent agreement with our background estimate. The overall rate of correlated background events that pass the IBD cuts is independently verified by analyzing 22.5 hours of both-reactors-off data. The expected neutrino signal is < 0.3 residual $\bar{\nu}_e$ events. Three events passed the first 4 cuts in Section V A. Two events with prompt energies of 4.8 MeV and 9.4 MeV were associated within 30 cm and 240 ms with the closest energetic muon, and are thus likely to be associated with ^{9}Li. Indeed, the second candidate is rejected by the showering muon veto. The third candidate at a prompt energy of 0.8 MeV features 3.5 m distance between prompt and delayed events and is therefore most likely a random coincidence. Immediately following the data set used in this paper, we obtained a larger data set with both-reactors-off. That will be the subject of a separate paper [59].
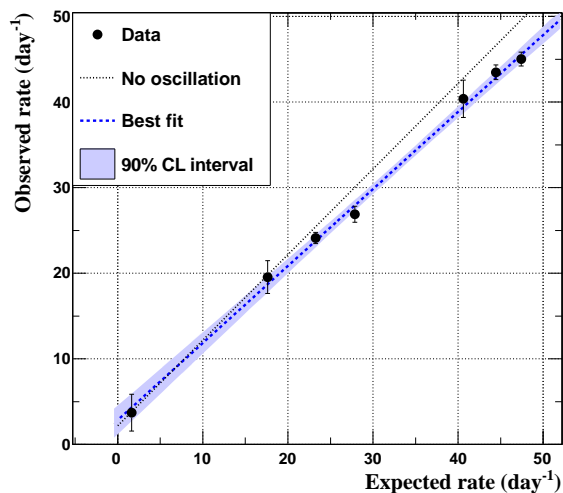

FIG. 12. Daily number of $\bar{\nu}_e$ candidates as a function of the expected number of $\bar{\nu}_e$. The dashed line shows the fit to the data, along with the 90% C.L. band. The dotted line shows the expectation in the no-oscillation scenario.

F. Neutron Detection Efficiency

Calibration data taken with the ^{252}Cf source were used to check the Monte Carlo prediction for any biases in the neutron selection criteria and estimate their contributions to the systematic uncertainty.

The fraction of neutron captures on gadolinium is evaluated to be 86.5% near the center of the target, 1.5% lower than the fraction predicted by simulation. Therefore the Monte Carlo simulation for the prediction of the number of $\bar{\nu}_e$ events is reduced by factor of 0.985. After the prediction of the fraction of neutron captures on gadolinium is scaled to the data, the prediction reproduces the data to within 0.3% under variation of selection criteria.

The ^{252}Cf is also used to check the neutron capture time, ΔT. The time difference between the prompt event and neutron capture signal for the californium calibration data is shown in Figure 13. The simulation reproduces the efficiency (96.2%) of the Δt_{e^+n} cut with an uncertainty of 0.5% augmented with sources deployed through the NT and GC.

The efficiency for Gd capture events with visible energy greater than 4 MeV to pass the 6 MeV cut is estimated to be 94.1%. Averaged over the NT, the fraction of neutron captures on Gd accepted by the 6.0 MeV cut is in agreement with calibration data to within 0.7%.

The Monte Carlo simulation indicates that the number of IBD events occurring in the GC with the neutron captured in the NT (spill-in) slightly exceeds the number of events occurring in the target with the neutron escaping to the gamma catcher (spill-out), by $1.35\% \pm 0.04\%$(stat) $\pm 0.30\%$(sys). The spill-in/out effect is already included in the simulation and therefore no correction for this is needed. The uncertainty of 0.3% assigned to the net spill-in/out current was quantified by varying the parameters affecting the process, such as gadolinium concentration in the target scintillator and hydrogen fraction in the gamma-catcher fluid within its tolerances. Moreover the parameter variation was performed with multiple Monte Carlo models at low neutron energies.

VI. OSCILLATION ANALYSIS

The oscillation analysis is based on a combined fit to antineutrino rate and spectral shape. IBD candidates are selected as described in Section V A. The data are compared to the Monte Carlo signal and background events from high-statistics samples. The same selections are applied to both signal and background, with corrections made to Monte Carlo only when necessary to match detector performance metrics.

The oscillation analysis begins by separating the data into 18 variably-sized bins between 0.7 and 12.2 MeV. Two integration periods are used in the fit to help separate background and signal flux. One set contains data periods where one reactor is operating at less than 20% of
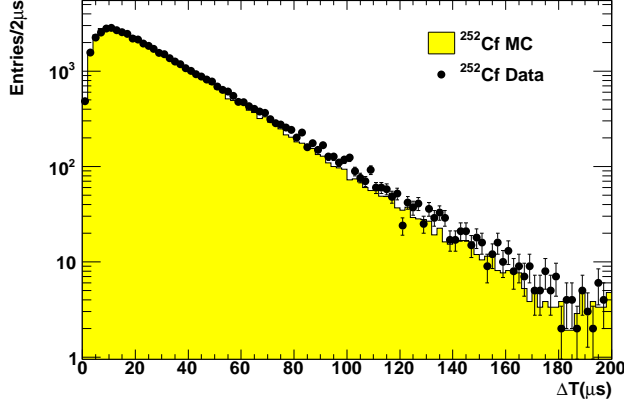
FIG. 13. Time difference between prompt and delayed events with ^{252}Cf at the detector center. The prompt time is determined by 7-30 MeV gamma ray.

	Reactors Both On	One Reactor $P_{th} < 20\%$	Total
Livetime [days]	139.27	88.66	227.93
IBD Candidates	6088	2161	8249
ν Reactor B1	2910.9	774.6	3685.5
ν Reactor B2	3422.4	1331.7	4754.1
Cosmogenic Isotope	174.1	110.8	284.9
Correlated FN & SM	93.3	59.4	152.7
Accidentals	36.4	23.1	59.5
Total Prediction	6637.1	2299.7	8936.8

TABLE V. Summary of observed IBD candidates, with corresponding signal and background predictions for each integration period, before any oscillation fit results have been applied.

its nominal thermal power, according to power data provided by EDF, while the other set contains data from all other times, typically when both reactors are running. All data end up in one of the two integration periods. Here, we denote the number of observed IBD candidates in each of the bins as N_i, where i runs over the combined 36 bins of both integration periods. The use of multiple periods of data integration takes advantage of the different signal/background ratios in each period, as the signal rate varies with reactor power while the backgrounds remain constant in time. This technique adds information about background behavior to the fit. The distribution of IBD candidates between the two integration periods is given in Table V.

A prediction of the observed number of signal and background events is constructed for each energy bin, following the same integration period division as the data:

$$N_i^{\text{pred}} = \sum_{R=1,2}^{\text{Reactors}} N_i^{\nu,R} + \sum_{b}^{\text{Bkgnds.}} N_i^b \qquad (13)$$

where $N_i^{\nu,R} = P_{(\bar{\nu}_e \to \bar{\nu}_e)} N_i^{\text{exp},R}$; $P_{\bar{\nu}_e \to \bar{\nu}_e}$ is the neutrino survival probability from the well-known oscillation formula and $N_i^{\text{exp},R}$ is given by Equation 4. The index b runs over the three backgrounds: cosmogenic isotope; correlated; and accidental. The index R runs over the two reactors, Chooz B1 and B2.

Background populations were calculated based on the measured rates and the livetime of the detector during each integration period. Details on the signal prediction normalization can be found in Sec. III D. Predicted populations for both null-oscillation signal and backgrounds may be found in Table V.

Systematic and statistical uncertainties are propagated to the fit by the use of a covariance matrix M_{ij} in order to properly account for correlations between energy bins.

The sources of uncertainty A are listed in Table VI.

$$M_{ij} = M_{ij}^{\text{sig.}} + M_{ij}^{\text{det.}} + M_{ij}^{\text{stat.}} + M_{ij}^{\text{eff.}} + \sum_{b}^{\text{Bkgnds.}} M_{ij}^{\text{b}} \qquad (14)$$

Each term $M_{ij}^{\text{A}} = \text{cov}(N_i^{\text{pred}}, N_j^{\text{pred}})_A$ on the right-hand side of Equation 14 represents the covariance of N_i^{pred} and N_j^{pred} due to uncertainty A. The normalization uncertainty associated with each of the matrix contributions may be found from the sum of each matrix: these are summarized in Table VI. Many sources of uncertainty contain spectral shape components which do not directly contribute to the normalization error, but do provide for correlated uncertainties between the energy bins. The signal covariance matrix $M_{ij}^{\text{sig.}}$ is calculated taking into account knowledge about the predicted neutrino spectra. The ^{9}Li matrix contribution contains spectral shape uncertainties estimated using different Monte Carlo event generation parameters, as described in Sec. III E. The slope of the FN/SM spectrum is allowed to vary from a nearly-flat spectrum following the measurements described in Section V D. Since accidental background uncertainties are measured to a high precision from many off-time windows, they are included as a diagonal covariance matrix.

The elements of the covariance matrix contributions are recalculated as a function of the oscillation and other parameters (see below) at each step of the minimization. This maintains the fractional systematic uncertainties as the bin populations vary from the changes in the oscillation and fit parameters.

A fit of the binned signal and background data to a two-neutrino oscillation hypothesis was performed by

Source	Uncertainty [%]
Reactor Flux	1.67%
Detector Response	0.32%
Statistics	1.06%
Efficiency	0.95%
Cosmogenic Isotope Background	1.38%
FN/SM	0.51%
Accidental Background	0.01%
Total	2.66%

TABLE VI. Summary of signal and background normalization uncertainties in this analysis relative to the total prediction.

minimizing a standard χ^2 function:

$$\chi^2 = \sum_{i,j}^{36} \left(N_i - N_i^{\text{pred}} \right)$$
$$\times \left(M_{ij} \right)^{-1} \left(N_j - N_j^{\text{pred}} \right)^{\text{T}}$$
$$+ \frac{\left(\epsilon_{FN/SM} - 1 \right)^2}{\sigma_{FN/SM}^2} + \frac{\left(\epsilon_{9\text{Li}} - 1 \right)^2}{\sigma_{9\text{Li}}^2}$$
$$+ \frac{\left(\alpha_E - 1 \right)^2}{\sigma_{\alpha_E}^2} + \frac{\left(\Delta m_{31}^2 - \left(\Delta m_{31}^2 \right)_{\text{MINOS}} \right)^2}{\sigma_{\text{MINOS}}^2} \quad (15)$$

The use of energy spectrum information in this analysis allows additional information on background rates to be gained from the fit, in particular because of the small number of IBD events between 8 and 12 MeV. The two fit parameters $\epsilon_{FN/SM}$ and $\epsilon_{9\text{Li}}$ are allowed to vary as part of the fit, and they scale the rates of the two backgrounds (correlated and cosmogenic isotope). The rate of accidentals is not allowed to vary since its initial uncertainty is precisely determined by the measurement method described in Sec. V B. The energy scale for predicted signal and ^{9}Li events is allowed to vary linearly according to the α_E parameter with an uncertainty $\sigma_{\alpha_E} = 1.13\%$. A final parameter constrains the mass splitting Δm_{31}^2 using the MINOS measurement [60] of $\Delta m_{31}^2 = (2.32 \pm 0.12) \times 10^{-3}$ eV^2, where we have symmetrized the error. This error includes the uncertainty introduced by relating the effective mass-squared difference observed in a ν_μ disappearance experiment to the one relevant for reactor experiments, and the ambiguity due to the type of the neutrino mass hierarchy, see e.g. [61]. Uncertainties for these parameters, $\sigma_{FN/SM}$, σ_{9Li}, and σ_{MINOS}, are listed as the initial values in Table VII.

The best-fit gives $\sin^2 2\theta_{13} = 0.109 \pm 0.030$ (stat.) $\pm$ 0.025 (syst) at $\Delta m_{31}^2 = 2.32 \times 10^{-3}$ eV^2, with a $\chi^2/\text{NDF} = 42.1/35$. We used the MINOS measured Δm_{31}^2 value as a constraint for our θ_{13} measurement, but a two parameter fit without the MINOS Δm_{31}^2 in the region $\Delta m_{31}^2 < 0.01$ eV^2 gives a Δm_{31}^2 value of $2.7 \pm 1.9 \times 10^{-3}$ eV^2, which is fully consistent with MINOS. The fit gives $\sin^2 2\theta_{13} = 0.093 \pm 0.078$ which is consistent with our fit for θ_{13} using MINOS.

Table VII gives the resulting values of the fit parameters and their uncertainties. Comparing the values with the ones used as input to the fit in Table V we conclude that the background rate and uncertainties are further constrained in the fit, as well as the energy scale.

The final measured spectrum and the best-fit spectrum are shown in Figure 14 for the new and old data sets, and for both together in Figure 15.

Fit Parameter	Initial Value	Best-Fit Value
^{9}Li Bkg. $\epsilon_{9\text{Li}}$	(1.25 ± 0.54) d^{-1}	(1.00 ± 0.29) d^{-1}
FN/SM Bkg. $\epsilon_{FN/SM}$	(0.67 ± 0.20) d^{-1}	(0.64 ± 0.13) d^{-1}
Energy Scale α_E	1.000 ± 0.011	0.986 ± 0.007
Δm_{31}^2 $(10^{-3}$ eV$^2)$	2.32 ± 0.12	2.32 ± 0.12

TABLE VII. Parameters in the oscillation fit. Initial values are determined by measurements of background rates or detector calibration data. Best-fit values are outputs of the minimization procedure.

An analysis comparing only the total observed number of IBD candidates in each integration period to the expectations produces a best-fit of $\sin^2 2\theta_{13} = 0.170 \pm 0.052$ at $\chi^2/\text{NDF} = 0.50/1$. The compatibility probability for the rate-only and rate+shape measurements is about 30% depending on how the correlated errors are handled between the two measurements.

A re-processing of the data set used for the first Double Chooz publication [7] was performed using the current analysis techniques. A fit using only a single integration period yielded a best-fit value of $\sin^2 2\theta_{13} = 0.0744 \pm 0.046$ with $\chi^2/\text{NDF} = 18.3/17$. An analysis of only the data taken since the first publication yielded a best-fit of $\sin^2 2\theta_{13} = 0.143 \pm 0.043$ with $\chi^2/\text{NDF} = 9.54/17$. The data and best-fit spectra for each of these cases is shown in Figure 16.

Our predicted fission cross section is $5.723 \pm 0.096 \times 10^{-43}$ cm^2/fission using the Bugey4 anchoring measurement and corresponding to the values of α_k in Table I. The background subtracted reactor antineutrino event rate is 7751.9 events, corresponding to 91.85% of the rate expected in the absence of oscillations. Our measured fission cross section is 5.257 ± 0.056 (stat.) ± 0.105 (syst) $\times 10^{-43}$ cm^2/fission.

A further cross-check of the analysis was carried out by imposing cuts to eliminate the vast majority of the cosmogenic isotope background at the cost of reduced livetime. The best-fit case of this analysis was found at $\sin^2 2\theta_{13} = 0.109 \pm 0.044$ and $\Delta m_{31}^2 = 2.32 \times 10^{-3}$ eV^2, in good agreement with the standard analysis.

Confidence intervals for the standard analysis were determined using a frequentist technique [62]. This approach accommodates the fact that the true χ^2 distributions may not be Gaussian and is useful for calculating the probability of excluding the no-oscillation hypothesis. This study compared the data to 10,000 simulations generated at each of 21 test points in the range $0 \leq \sin^2 2\theta_{13} \leq 0.25$. A $\Delta\chi^2$ statistic, equal to the difference between the χ^2 at the test point and the χ^2 at
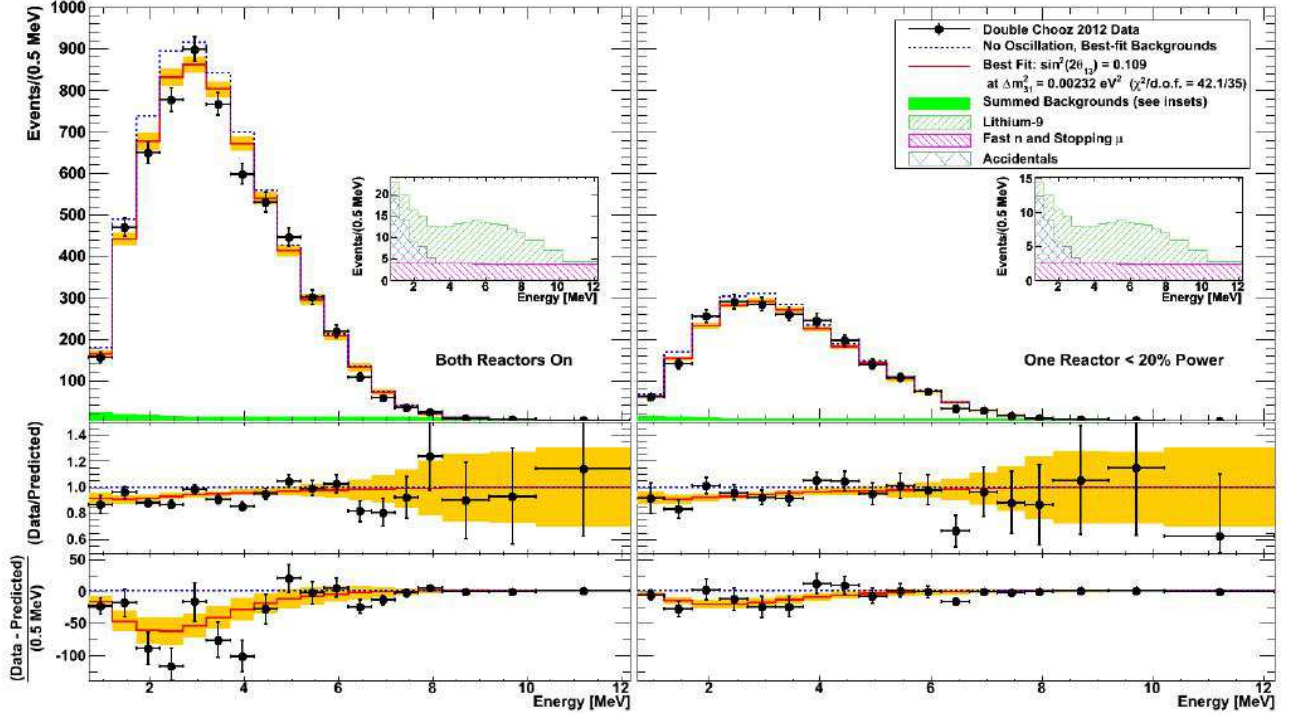
FIG. 14. Measured prompt energy spectrum for each integration period (data points) superimposed on the expected prompt energy spectrum, including backgrounds (green region), for the no-oscillation (blue dotted curve) and best-fit (red solid curve) at $\sin^2 2\theta_{13} = 0.109$ and $\Delta m_{31}^2 = 2.32 \times 10^{-3}$ eV^2. Inset: stacked spectra of backgrounds. Bottom: differences between data and no-oscillation prediction (data points), and differences between best fit prediction and no-oscillation prediction (red curve). The orange band represents the systematic uncertainties on the best-fit prediction.
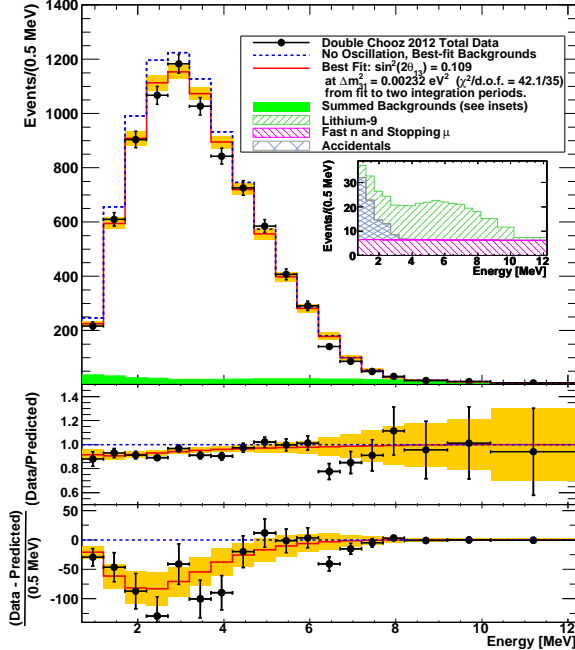
FIG. 15. Sum of both integration periods plotted in the same manner as Figure 14.

the best fit, was used to determine the region in $\sin^2 2\theta_{13}$

where the $\Delta\chi^2$ of the data was within the given confidence probability. The allowed region at 68% (90%) CL is 0.067 $(0.043) < \sin^2 2\theta_{13} < 0.15$ (0.18). An analogous technique shows that the data excludes the no-oscillation hypothesis at 99.8% (2.9σ).

VII. CONCLUSION

A comparison of this analysis result to other recent $\sin^2 2\theta_{13}$ measurements by other experiments is shown in Figure 17. The figure shows published results, though we note that new results from Daya Bay, MINOS and T2K have been shown at conferences but are not yet published [63]. The values for $\sin^2 2\theta_{13}$ from the various experiments are in excellent agreement with the results reported here. However this result is unique in its incorporation of energy dependence in the analysis.

Double Chooz has found evidence for a non-zero value of θ_{13} from the rate and energy spectrum of reactor neutrino candidates at a distance of 1050 m from two reactors. It is the first evidence for this parameter using the energy spectrum from reactor neutrinos, rather than simply their rate. We find a best fit value and 1σ error to be $\sin^2 2\theta_{13} = 0.109 \pm 0.030$ (stat) $\pm$ 0.025 (syst). The data is inconsistent with the assumption that oscillations
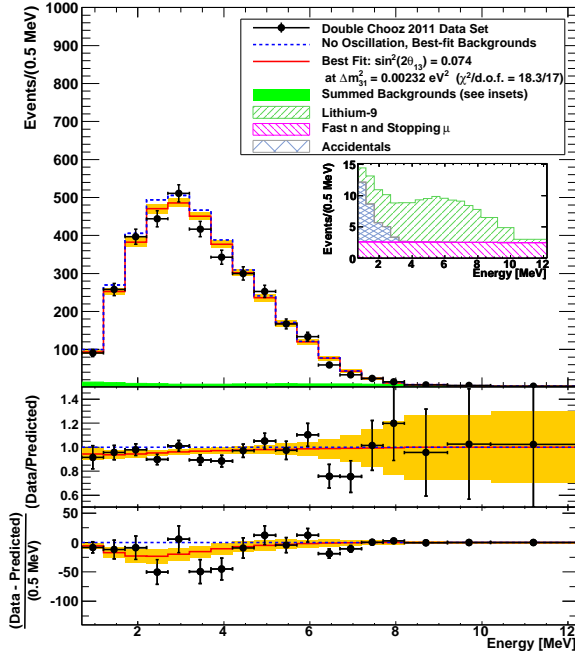
(a)First Publication Data Set
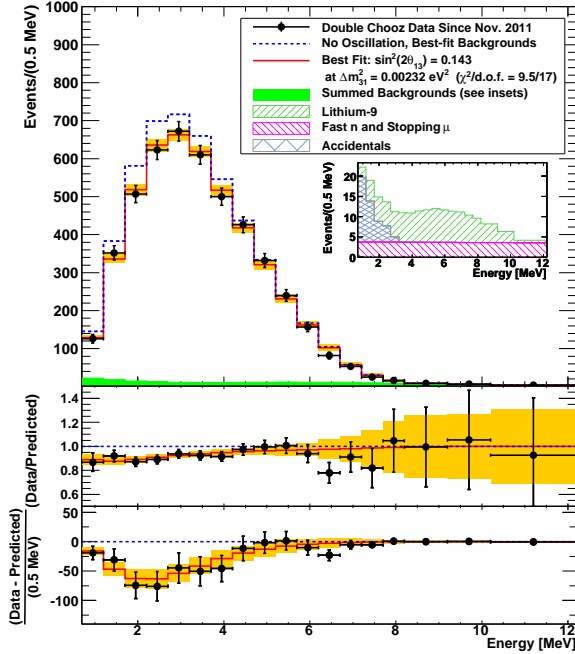
(b)Data Since First Publication

FIG. 16. Data and best-fit spectrum from applying current analysis techniques to the data set used to produce the first Double Chooz publication (a), and data taken since that publication (b), plotted in the same manner as Figure 14.
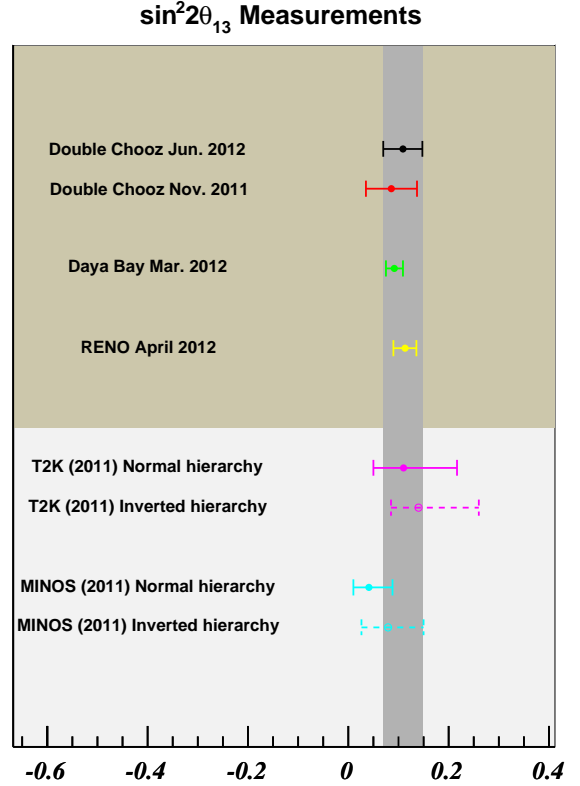

FIG. 17. Comparison of recent reactor- and accelerator-based measurements of $\sin^2 2\theta_{13}$ from this analysis, the first Double Chooz publication [7], Daya Bay [8], RENO [9], T2K [6], and MINOS [5]. Error bars correspond to 1σ. For T2K and MINOS the CP phase δ has been fixed (arbitrarily) to $\delta = 0$.

are absent with a CL of 99.8% CL (2.9σ).

[1] M. Appolonio et al., Phys. Lett., B466, 415 (1999).
[2] G. L. Fogli, E. Lisi, A. Marrone, A. Palazzo and A. M. Rotunno, Phys. Rev. D84, 053007 (2011).
[3] The KamLAND Collaboration, Phys. Rev. D83, 052002 (2011).
[4] T. Schwetz et al., New J. Phys. 13, 109401 (2011).
[5] P. Adamson et al., Phys. Rev. Lett. 107, 181802 (2011).
[6] K. Abe et al., Phys. Rev. Lett. 107, 041801 (2011).
[7] Y. Abe et al., Phys. Rev. Lett. 108, 131801 (2012).
[8] F. P. An et al., Phys. Rev. Lett. 108, 171803 (2012).
[9] J. K. Ahn et al., Phys. Rev. Lett. 108, 191802 (2012).
[10] F. Ardellier et al., (Double Chooz Collaboration) (2006) hep-ex/0606025.
[11] T. Matsubara et al., Nucl. Instrum. Meth., A661, 16, 2011.
[12] C. Bauer et al., JINST, 6, P06008 (2011).
[13] E. Calvo et al., Nucl. Instrum. Meth., A621, 222 (2010).
[14] M. Fechner et al., Applied Radiation and Isotopes, 69(7), 1033 (2011).
[15] G. Heusser, M. Laubenstein, H. Neder, Radionuclides in the environment, Int. Conf. on Isotopes in Environmental Studies, edited by P. P. Povinec and J. A. Sanchez-Cabeza, Elsevier, Amsterdam 495 (2006).
[16] C. Aberle et al., JINST, 7, P06008 (2012).
[17] M. Hofmann, Ph.D. thesis, Technische Universität München (2012).
[18] Measured by A. Smith at the LBNL Low Background Facility with the MERLIN n-type HPGe detector.
[19] S. Abe et al., Phys. Rev. C81, 025807 (2010).
[20] M. Apollonio et al., Eur. Phys. J, C27, 331 (2003).
[21] C. Aberle, C. Buck, F.X. Hartmann and S. Schönert, Chem. Phys. Lett., 516, 257 (2011).
[22] http://jp.hamamatsu.com/resources/products/etd /pdf/LARGE_AREA_PMT_TPMH1286E05.pdf.
[23] F. Kaether and C. Langbrandtner, arXiv:1207.0378 (submitted to JINST).
[24] D. Dietrich et. al. "Monte Carlo aided design of the Inner Muon Veto detectors for the Double Chooz experiment" (2012), accepted for publication in JINST.
[25] K. Zbiri, arXiv:1104.4045 (2011).
[26] Max Perles et cie, http://www.maxperles.com/pdf /ftech_fr/ft_ar100clx_nov10.pdf (2012).
[27] F. Beissel et al., "The Trigger and Timing System of the Double Chooz Experiment" (submitted to JINST).
[28] A. Cabrera, Nucl. Instrum. Meth. Phys. Res., Sect. A 617, 473 (2010).
[29] T. Akiri, Ph.D. thesis, Universite Paris-Diderot, (2010).
[30] CAEN Corporation, http://www.caen.it/. The device was co-developed with APC.
[31] P. Barrillon et al., MAROC: Multi-Anode ReadOut Chip for MAPMTs, proceedings of 2007 IEEE conference (2007), P. Barrillon et al., 64-channel Front-End readout chip, MAROC2 datasheet, http://omega.in2p3.fr/.
[32] E. Tournu et al., EDF TechnicalNote (2001).
[33] Standard AFNOR XP X 07-020 (1996).
[34] Y. Caffari, J.M. Favennec, EDF tech-note H-P1C-2011-02007-FR.
[35] Z. Djurcic et al., J. Phys. G36, 045002 (2009).
[36] K. Schreckenbach, G. Colvin, and F. von Feilitzsch, Phys. Lett. 160B, 325 (1985).
[37] F. von Feilitzsch and K. Schreckenbach, Phys. Lett. 118B, 162 (1982).
[38] A. Hahn et al., Phys. Lett. B 218, 365 (1989).
[39] T. Mueller et al., Phys. Rev. C83, 054615 (2011).
[40] P. Huber, Phys. Rev. C84, 024617 (2011).
[41] G. Mention et al., Phys. Rev. D83, 073006 (2011).
[42] O. Meplan et al., in ENC 2005: European Nuclear Conference; Nuclear power for the XXIst century: from basic research to high-tech industry (2005).
[43] NEA-1845/01, documentation for MURE (2009).
[44] G. Marleau et al., Report IGE-157 (1994).
[45] C. Jones, "Prediction of the Reactor Antineutrino Flux for the Double Chooz Experiment", Ph.D. thesis, MIT (2012).
[46] C. Jones et al., arXiv:1109.5379v1 (2011).
[47] V. Kopeikin, L. Mikaelyan, and V. Sinev, Phys. At. Nucl. 67, 1892 (2004).
[48] Y. Declais et al., Phys. Lett. B338, 383 (1994).
[49] P. Vogel and J. F. Beacom, Phys. Rev. D60, 053003 (1999).
[50] A. Pichlmaier et al., Phys. Lett. B693, 221 (2010).
[51] J. Allison et al., IEEE Trans. Nucl. Sci. 53 No. 1, 270 (2006), S. Agostinelli et al., Nucl. Instrum. Meth. A506, 250 (2003).
[52] J. Apostolakis et al., "Geant4 Physics Lists for HEP," Nuclear Science Symposium Conference Record, IEEE, 833 (2008).
[53] J.B. Birks, Proc. Phys. Soc. A64, 874 (1951); 64, 511 (1951).
[54] D. Motta and S. Schönert, Nucl. Instrum. Meth. A539, (2005) 217.
[55] D. R. Tilley et al., Nucl. Phys. A745, 155 (2004), Y. Prezado, et al., Physics Letters B618, 43.50 (2005), P. Papka, et al., Phys. Rev. C 75, 045803 (2007).
[56] http://www.chem.agilent.com/en-US/Products/instruments/molecularspectroscopy/fluorescence/systems/caryeclipse/pages/default.aspx.
[57] C. Aberle, C. Buck, F.X. Hartmann, S. Schönert and S. Wagner, JINST 6, P11006 (2011).
[58] C. Aberle, Ph.D. thesis, Universität Heidelberg (2011).
[59] Y. Abe et al., in preparation.
[60] P. Adamson et al., Phys. Rev. Lett. 106, 181801 (2011).
[61] H. Nunokawa, S. Parke and R.Z. Funchal, Phys. Rev. D72, 013009 (2005).
[62] G.J. Feldman and R.D. Cousins, Phys. Rev. D57, 3873 (1998).
[63] Proceedings of the XXXV International Conference on Neutrino Physics and Astrophysics, June 3-9, 2012, Kyoto, Japan, to be published.